



Determination of voltage condition for target displacement field of dielectric elastomer actuator using artificial neural network

Ki Hyun Kim¹ · Gil Ho Yoon¹

Received: 21 December 2022 / Revised: 6 April 2023 / Accepted: 15 May 2023 / Published online: 8 June 2023
© The Author(s), under exclusive licence to Springer-Verlag GmbH Germany, part of Springer Nature 2023

Abstract

In this study, we explore the feasibility of the artificial neural network (ANN) model in the inverse problem that determines the voltage condition for implementing a desired deformation of the dielectric elastomer actuator (DEA). Our main focus is on the effectiveness of two basic approaches based on supervised learning in the inverse problem of DEA. In the first approach, the forward problem of computing the vertical displacement field of DEA using finite element analysis (FEA) is replaced by ANN. Then, a genetic algorithm (GA) is employed to find the optimal voltage condition using the ANN for forward mapping. In the second approach, the inverse problem is directly solved using the ANN for inverse mapping. Although a supervised learning-based approach requires a data generation process and is data-dependent, it can be considered as an easy-to-use tool for a variety of engineering problems and can be the basis for applying advanced optimization techniques. In the present work, a bilayer DEA with segmented regions for different voltage applications is considered to implement various curved deformations. In terms of conducting an initial study, voltage conditions are simply expressed as a 3×3 matrix and displacement fields as a 12×12 matrix. To compare the two approaches, an example of finding the voltage condition that similarly imitates an arbitrary target displacement field is provided. The first approach is better in terms of accuracy when the target displacement field is abstract and far from the characteristics of the training data of ANN. Conversely, the second approach is better in terms of real-time prediction when the target displacement field is more realistically generable.

Keywords Dielectric elastomer actuator · Inverse problem · Artificial neural network · Supervised learning

1 Introduction

With the development of artificial neural network (ANN)-based machine learning techniques, so-called deep learning, data-driven models have recently been widely applied to computational physics and design optimization. Typically, ANN has been used as an approximate prediction model, i.e., a surrogate model, to replace time-consuming numerical analysis. In particular, distributed physical properties have been successfully predicted using ANNs. For example, a velocity field of non-uniform steady laminar flow was predicted by a convolutional neural network (CNN) using a data

set from computational fluid dynamics (Guo et al. 2016). Regarding the structural finite element analysis (FEA), a stress distribution in the aortic wall was predicted by a multilayer neural network (Liang et al. 2018). In another paper, a stress field of a two-dimensional cantilevered structure was predicted using CNN (Nie et al. 2020). These studies mainly used geometric shape information of the target object as an input to the ANN. Furthermore, ANN has been used as a tool for real-time generation of optimal designs (Yu et al. 2019; Lei et al. 2019; Zheng et al. 2021). The ANNs used in these studies are classified as supervised learning. In addition to supervised learning, ANNs for reinforcement learning, another category of machine learning, have also been recently applied to engineering design problems (Lee et al. 2019; Sui et al. 2021; Brown et al. 2022). All the mentioned studies prove that ANNs are a very effective tool for engineering problems and can be applied in various ways depending on the purpose of use.

In relation to this study, ANNs have recently been used for the inverse problem, i.e., inverse design. The inverse

Responsible Editor: Zhen Hu.

✉ Gil Ho Yoon
ghy@hanyang.ac.kr

¹ School of Mechanical Engineering, Hanyang University,
222, Wangsimni-ro, Seongdong-gu, Seoul 04763,
South Korea

problem requires a proper strategy to solve it due to the burden of computational time required for iterative analysis process. The methods of utilizing ANNs in inverse problems can be divided into two approaches. The first approach is to use an ANN as a forward mapping, i.e., a surrogate model in the optimization process (Messner 2020; Weeratunge et al. 2022; Deng et al. 2022; Sun et al. 2022). If the FEA of the forward problem can be replaced with a surrogate model for instantaneous calculation, the inverse problem can be solved more effectively through optimization algorithms. The second approach is to use an ANN as an inverse mapping that provides an answer directly (Kumar and Vadlamani 2021; Zhang et al. 2019; Liu et al. 2018). In the literature (Kumar and Vadlamani 2021), CNN and deep neural network were used in the inverse design of the airfoil shapes for the target pressure distribution. In the literature (Zhang et al. 2019), both ANNs for forward and inverse mapping were presented for spectrum prediction and inverse design of structural parameters in plasmonic waveguide systems. In the literature (Liu et al. 2018), a pre-trained network for forward mapping was attached to the network for inverse mapping to solve the non-unique mapping in the inverse problem.

In this study, ANN-based supervised learning is used to solve the inverse problem of the dielectric elastomer actuator (DEA) with complex deformation through the computational time efficiency of ANN. DEA is a kind of lightweight and soft material that can be actuated by voltage application. DEA is a promising material for applications such as soft robots, wearable sensors, energy harvesters. It has been reported that machine learning techniques are used to enhance the capability of such applications of DEA (Ye and Chen 2017; Larson et al. 2019; Shih et al. 2020; Ashouri et al. 2022). However, as far as the authors know, few studies have used ANNs in determining the complex voltage condition of multiple electrodes to implement a specific displacement field of DEA.

1.1 Existing studies on DEA

DEAs are mechanically deformed under an electric field. Figure 1a illustrates this phenomenon in a simple DEA. One layer of a thin sheet of dielectric elastomer exists and two electrodes of very thin thickness are attached to the top and bottom surfaces of the dielectric elastomer. When a voltage, i.e., electric potential difference V_{diff} , is applied to the electrodes, the electrostatic attraction between the charges induces the Maxwell stress, which causes the dielectric elastomer layer to contract in the direction of thickness and expand to the lateral directions (Pelrine et al. 1998, 2000). The degree of expansion increases as the voltage increases. On the other hand, when two layers of dielectric elastomer are subjected to different voltages by three electrodes as depicted in Fig. 1b, different degrees

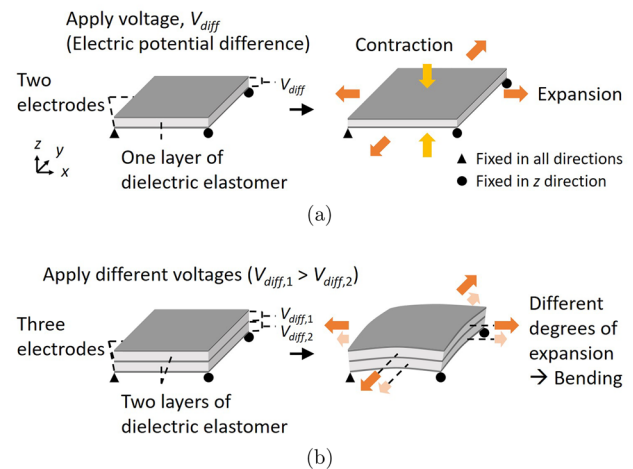


Fig. 1 Behaviors of **a** the DEA with one layer subjected to a voltage and **b** the DEA with two layers subjected to different voltages

of expansion in two layers induce bending deformation (Shian et al. 2015; Henann et al. 2013; Duduta et al. 2016; Hajiesmaili and Clarke 2019).

Various forms of DEAs have been developed to increase the applicability of DEA. For example, a DEA was formed into a cylindrical tube to take advantage of the lateral expansion of DEA (Carpi and De Rossi 2004). On the contrary, a folded form of continuous DEA using the shrinkage of thickness was suggested as a linear contractile actuator (Carpi et al. 2007). In a similar way, a novel helical configuration of DEA was also presented (Carpi et al. 2005). In some studies, dielectric elastomers were geometrically constrained to devise a hydrostatically coupled DEA system (Shian et al. 2013; Wang et al. 2012; Carpi et al. 2011). As a somewhat different concept, a pre-stain DEA was presented to produce various deformation shapes (Kofod et al. 2006). These mentioned studies basically used one layer of dielectric elastomer.

In a study for a bilayer elastomer, bending deformation of DEA was implemented using a passive elastomer sheet which is bonded to an active elastomer sheet having electrodes on both sides (Shian et al. 2015). The finite element formulation for bending deformation of the bilayer DEA was studied in the literature (Henann et al. 2013). With regard to multilayer elastomers, it has been suggested to vary the pattern of electrodes between different elastomer layers to create multimorph deformation (Duduta et al. 2016). The potential of multilayer elastomers to create complex deformation shapes was demonstrated by experiments and FEA in the literature (Hajiesmaili and Clarke 2019), where a spatially varying internal electric field was generated in the DEA using different shapes of electrodes that separate the elastomer layers.

Existing studies have dealt with the electrode shape and arrangement through sets of electrodes to implement various deformation of DEA (Duduta et al. 2016; Hajiesmaili and Clarke 2019; Ashouri et al. 2022). In these studies, a single voltage was selectively applied to some of electrodes, but different voltages were not applied to each electrode. They did not deal with complex voltage conditions applied to DEA enough to use ANNs. On the other hand, in this study, different voltages are applied to each electrode regardless of the actual implementation possibility of DEA. In a paper on polymer sensors (Ashouri et al. 2022), electrode shapes were designed using a 5×5 divided area and the electrical resistance according to the electrode shape was predicted using ANNs. ANNs can map complex relationships effectively, so they can be used when the number of design variables is large. Therefore, we apply ANN to the problem of determining different voltages for multiple arranged electrodes to implement complex DEA deformation.

1.2 Inverse problem of DEA

As mentioned in the literature (Hajiesmaili and Clarke 2019), shape morphing with various Gaussian curvatures is possible by designing the geometry, position, and applied voltages of electrodes. However, designing such features of electrodes to create a target deformation shape is an intractable inverse problem. If considering only the voltages applied by multiple arranged electrodes without considering the geometry and position of the electrodes, the inverse problem of DEA can be simplified. Thus, this paper solves the inverse problem associated with the voltage condition determination of DEA for the target deformation shape.

In this study, we propose a bilayer DEA with multiple segmented regions for applying different voltages to implement various deformation shapes. As shown in Fig. 2, a voltage pair is applied to the top and bottom layers of each segmented region of the bilayer DEA. For a certain voltage condition, i.e., voltage pairs in multiple segmented regions, FEA is performed to obtain the deformation shape. As shown in Fig. 2, the deformation shape is colored with the vertical displacement field, i.e., z -direction displacement field, because the vertical displacement is dominant over the horizontal displacement in the presented DEA. Conceptually, obtaining the displacement field from the voltage condition is a forward problem corresponding to the analysis. Conversely, determining the appropriate voltage condition to implement the target displacement field is an inverse problem corresponding to the design.

This study uses two basic approaches for the inverse problem of the presented DEA. In the first approach, an ANN is used as a surrogate model to predict the displacement field of the DEA. Using the ANN for forward mapping, we search for a voltage condition that yields a

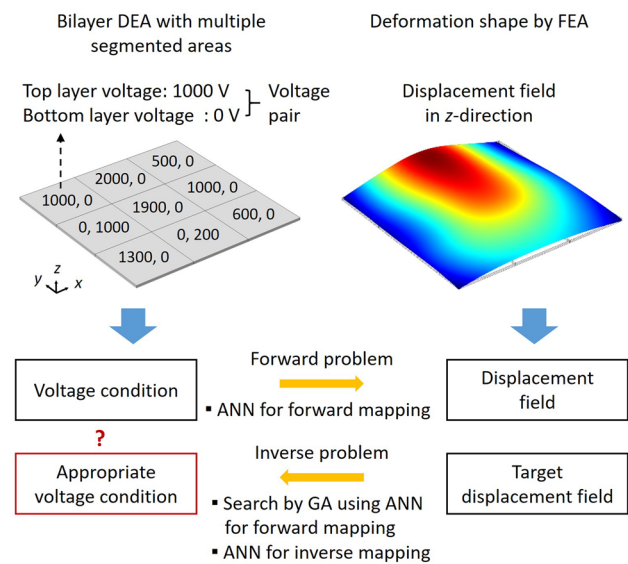


Fig. 2 Purpose of the present study

predicted displacement field that best fits the target displacement field. As a search method, well-known genetic algorithm (GA) is used. In the second approach, it is considered to construct an ANN for inverse mapping that directly predicts the appropriate voltage condition from the target displacement field. As will be discussed in our results, when a displacement field that cannot be accurately or approximately obtained through FEA is given as an input to the ANN for inverse mapping, it may be somewhat difficult to predict the appropriate voltage condition. It is also noted that constructing the ANN requires efforts to collect a training data set from FEA results for various voltage conditions. Nevertheless, this study pays attention to the point that the efficiency according to the use of ANN can offset the time consumption of preparing a data set. To the best of the authors' knowledge, no studies have been attempted to solve the inverse problem of bilayer DEA with multiple arranged electrodes with different voltages using ANN.

The remainder of this paper is organized as follows. Section 2 introduces the FEA for the bilayer DEA with multiple segmented regions. Section 3 describes how to generate the FEA data set for ANN construction. Section 4 provides the results of predicting the displacement field of DEA using the ANN for forward mapping. Section 5 presents examples of determining the voltage condition to imitate the target displacement field using the ANN for forward mapping and the GA. Section 6 address the direct determination of voltage condition using the ANN for inverse mapping. Sect. 7 investigates the effect of noise in the training data. Sect. 8 draws the conclusions of this study.

2 FEA of bilayer DEA

2.1 Physics equations of DEA

This section briefly introduces the FEA for obtaining the displacement field of the presented DEA. The FEA in the present study was performed by COMSOL Multiphysics, a commercial software. The presented FEA solves the electrostatics equation and the solid mechanics equation by coupling the two equations. In the electrostatics equation in Eq. (1), ϵ_0 , ϵ_r , and V denote the permittivity of vacuum, the relative permittivity, and the unknown electric potential, respectively. The boundary conditions used for the electrostatics equation are the zero charge in Eq. (2) and the constant electric potential in Eq. (3). Regarding the solid mechanics equation, the compressible version of the Neo-Hookean hyperelastic material model in Eq. (4) is used, where W_s , I_1 and J denote the strain energy density, the first invariant of the right Cauchy-Green deformation tensor, and the elastic volume ratio, respectively (Attard 2003). The parameter μ and λ denote the shear modulus and the first Lamé parameter. The boundary conditions used for the solid mechanics equation are the fixed point and the zero displacement in z -direction.

$$-\nabla \cdot (\epsilon_0 \epsilon_r \nabla V) = 0 \quad (1)$$

$$\mathbf{bfn} \cdot \nabla V = 0 \quad (2)$$

$$V = V_{\text{constant}} \quad (3)$$

$$W_s = \frac{1}{2} \mu (I_1 - 3) - \mu \ln(J) + \frac{1}{2} \lambda (\ln(J))^2 \quad (4)$$

In this study, the material properties of the dielectric elastomer is set to the values presented in the literature (Hajiesmaili and Clarke 2019), where the relative permittivity ϵ_r of 5.5, the shear modulus μ of 312 kPa, and the bulk modulus K of 32.2 MPa were presented. The first Lamé parameter λ was calculated from the shear and bulk moduli using the conversion formula of elastic materials as Eq. (5). The obtained value of the first Lamé parameter λ is 31.992 MPa. The coupled system of the electrostatics equation and the solid mechanics equation is solved by the damped Newton's method through a segregated approach. The solution for the unknown variables is obtained when the solution error is less than 0.001.

$$\lambda = K - \frac{2\mu}{3} \quad (5)$$

2.2 Preliminary test of FEA for basic DEAs

Prior to presenting the configuration of the DEA considered in this study, a preliminary test of the FEA was performed on the basic DEAs to confirm the validity of the used FEA. The first basic DEA is one layer of dielectric elastomer subjected to a single voltage as depicted in Fig. 3a (corresponding to Fig. 1a). The size of the first basic DEA is 0.005 m in x and y directions, and its thickness is 10^{-4} m. In order to apply a voltage to the layer, for example, electric potentials of 5000 V and 0 V are set on the top and bottom surfaces, respectively. The lateral surfaces are set to zero charge. The boundary conditions for displacement u are set at the vertices of the bottom surface. One vertex is set to zero displacement in all directions and the other three vertices are set to zero displacement in z -direction. If the displacement in z -direction u_z is not constrained to zero for the remaining three vertices, solutions having displacements of the three vertices close to 0 may not be obtained or the solution itself can not be obtained due to the nonlinear analysis. Therefore, the authors gave boundary conditions to the remaining vertices to obtain FEA data more reliably. To mesh the geometry, a rectangular parallelepiped element is used. The size of the element is 0.001 m in x and y directions and 5×10^{-5} m in z -direction. The element size is set relatively coarse within a range that satisfies the minimal mesh quality to shorten the analysis time. The reduction of analysis time is considered for future data set generation. In our own tests, the mesh size did not significantly affect the solution. The second basic DEA is a bilayer dielectric elastomer subjected to different voltages in each layer as depicted in Fig. 3b (corresponding to Fig. 1b). As the second basic DEA has two layers, its overall thickness is twice that of the first basic DEA. In order to apply different voltages to the two layers, for example, electric potentials of 2500 V, 0 V, and 500 V are set on the top, internal, and bottom surfaces, respectively.

Figure 4 shows the FEA results of the basic DEAs. First, Fig. 4a represents the deformation of the first basic DEA with the colored displacement fields in each direction. The first basic DEA exhibits an expanded deformation maintaining a flat top surface. In this case, the z -direction displacement has little effect on the deformation shape. Next, Fig. 4b represents the deformation of the second basic DEA. As can be seen from the z -direction displacement field, it exhibits a bending deformation with a curved top surface. In this case, the displacements in x and y directions have a relatively small effect on the deformation shape. These FEA results are consistent with the general behavior of DEA described in the introduction and show the validity of the FEA used.

Fig. 3 Basic DEAs with **a** one layer subjected to a voltage and **b** two layers subjected to different voltages

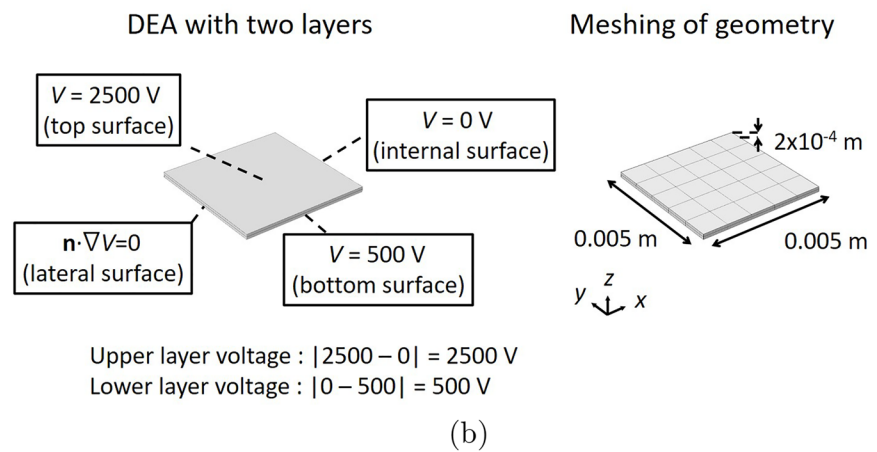
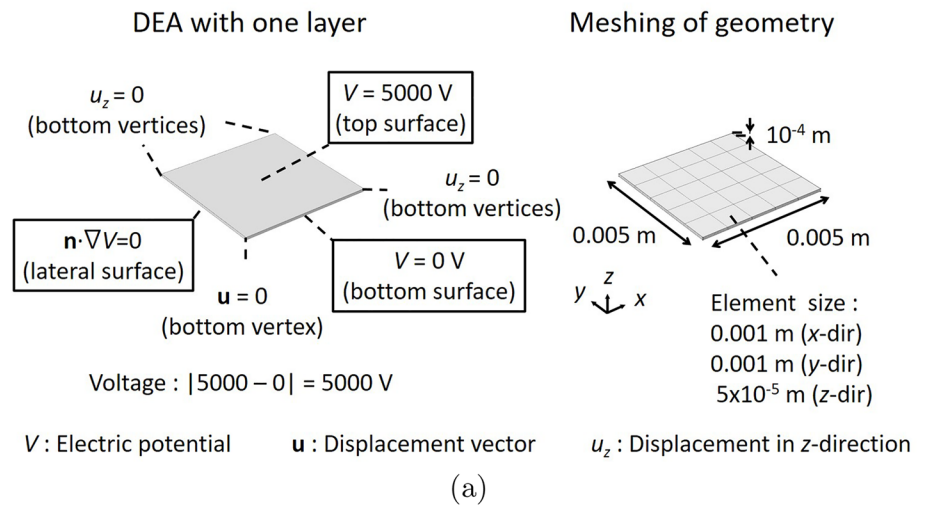
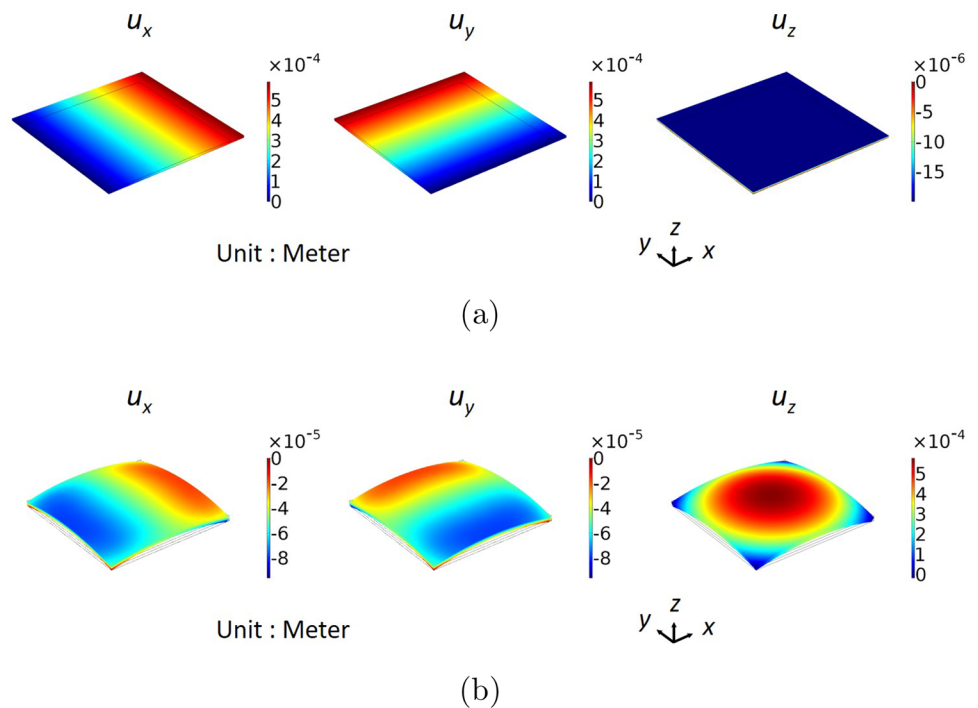


Fig. 4 FEA results of the basic DEAs with **a** one layer and **b** two layers



2.3 Bilayer DEA with multiple segmented regions

This study proposes a bilayer DEA with multiple segmented regions for different voltage applications as represented in Fig. 5. In the present work, only 9 segmented regions are considered for its simplicity and ease of obtaining FEA data. When the regions for voltage condition are set to 5×5 instead of 3×3 , it is more difficult to obtain a converged solution of FEA with an appropriate nonlinear solver configuration. That is, data collection for various voltage conditions is relatively difficult in the case of 5×5 regions. Therefore, in terms of data acquisition, the authors selected DEA with 3×3 segmented regions as the subject of this study. The size of the bilayer DEA is three times the size of the second basic DEA in x and y directions.

In our own tests, it has been observed that the difference in absolute voltage values between the two layers has a significant effect on the deformation of bilayer DEA. Thus, electric potentials of the segmented regions can be set in the following manner to simplify the voltage determination

problem. On the top surface of the DEA, different electric potentials (≥ 0 V) are set in the segmented regions. Here, electric potentials in some regions can be 0 V. On the internal surface, all electric potentials are set to 0 V. On the bottom surface, different electric potentials (> 0 V) are set only in the segmented regions where the electric potential in the corresponding segmented region on the top surface is 0 V. In the remaining regions on the bottom surface, electric potentials are set to 0 V. That means that one of the electric potentials of the top and bottom surfaces of the same region is set to 0 V.

Figure 6 shows the FEA result of the bilayer DEA with multiple segmented regions when the voltage condition is set as in Fig. 5. In this case, the deformation of the DEA represents an upward convex shape when viewed as a whole. Like the second basic DEA with two layers, the deformation shape is mainly affected by the z -direction displacement u_z . Although several examples are not provided here, when the voltage of the upper layer is higher than that of the lower layer in a local region, local deformation is likely

Fig. 5 Proposed DEA with multiple segmented regions

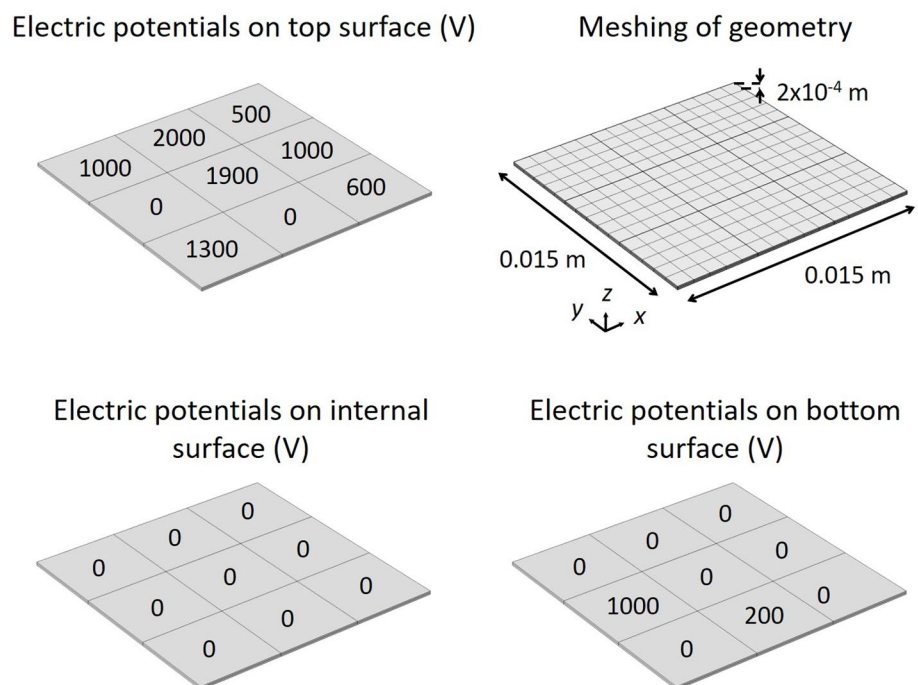
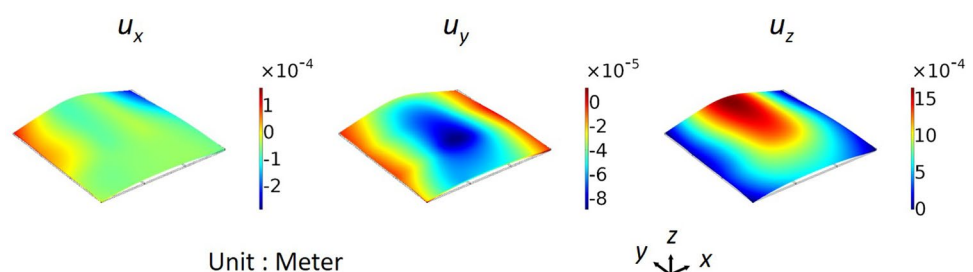


Fig. 6 FEA result of the proposed DEA with multiple segmented regions



to be convex upward. Conversely, when the voltage of the lower layer is higher than that of the upper layer in a local region, local deformation is likely to be convex downward. Of course, the exact deformation in a local region is determined by the voltage condition in the entire region. From the result of Fig. 6, it may be expected that deformation shape can be controlled more delicately by applying appropriate voltage condition to the multiple segmented regions.

3 Generation of data set for ANN construction

3.1 FEA under various voltage conditions

In this section, the FEA of the proposed DEA is performed under various voltage conditions to collect the data set needed to construct the ANNs. The setting method of electric potentials described in the Sect. 2.3 can be formulated as Eq. (6), where V_{top} , V_{internal} , and V_{bottom} represent the electric potentials on the top, internal, and bottom surfaces in each segmented region. Using the parameter a between 0 and 1, the electric potentials on the top and bottom surfaces are calculated within the maximum electric potential V_{max} . In this study, V_{max} is set to 2000 V considering numerical stability in FEA. For example, if the parameter a is set to 0.75, V_{top} and V_{bottom} are calculated as 1000 V and 0 V, respectively. In contrast, if the parameter a is set to 0.25, V_{top} and V_{bottom} are calculated as 0 V and 1000 V, respectively. If the parameter a is set to 0.5, both V_{top} and V_{bottom} are calculated as 0 V. It is noted that V_{top} and V_{bottom} cannot be greater than 0 V at the same time.

$$\begin{aligned} V_{\text{top}} &= \text{round}(V_{\text{max}} \times \max(2a - 1, 0)) \\ V_{\text{internal}} &= 0 \\ V_{\text{bottom}} &= \text{round}(V_{\text{max}} \times \max(-2a + 1, 0)) \end{aligned} \quad (6)$$

$(0 \leq a \leq 1)$

According to Eq. (6), the electric potentials of the 9 segmented regions are calculated using 9 values of a . Thus, a voltage condition matrix \mathbf{a} of size 3×3 is defined as Eq. (7) with elements between 0 and 1. Then, electric potential

matrices \mathbf{V}_{top} and $\mathbf{V}_{\text{bottom}}$ of size 3×3 are defined as Eqs. (8) and (9), respectively. Each element of \mathbf{V}_{top} and $\mathbf{V}_{\text{bottom}}$ are calculated from the corresponding element of the voltage condition matrix \mathbf{a} by Eq. (6). The elements of \mathbf{V}_{top} and $\mathbf{V}_{\text{bottom}}$ are assigned to the segmented regions as depicted in Fig. 7. Therefore, various voltage conditions can be generated simply using the voltage condition matrix \mathbf{a} .

$$\mathbf{a} = \begin{bmatrix} a^{1,1} & a^{1,2} & a^{1,3} \\ a^{2,1} & a^{2,2} & a^{2,3} \\ a^{3,1} & a^{3,2} & a^{3,3} \end{bmatrix} \quad (7)$$

$$\mathbf{V}_{\text{top}} = \begin{bmatrix} V_{\text{top}}^{1,1} & V_{\text{top}}^{1,2} & V_{\text{top}}^{1,3} \\ V_{\text{top}}^{2,1} & V_{\text{top}}^{2,2} & V_{\text{top}}^{2,3} \\ V_{\text{top}}^{3,1} & V_{\text{top}}^{3,2} & V_{\text{top}}^{3,3} \end{bmatrix} \quad (8)$$

$$\mathbf{V}_{\text{bottom}} = \begin{bmatrix} V_{\text{bottom}}^{1,1} & V_{\text{bottom}}^{1,2} & V_{\text{bottom}}^{1,3} \\ V_{\text{bottom}}^{2,1} & V_{\text{bottom}}^{2,2} & V_{\text{bottom}}^{2,3} \\ V_{\text{bottom}}^{3,1} & V_{\text{bottom}}^{3,2} & V_{\text{bottom}}^{3,3} \end{bmatrix} \quad (9)$$

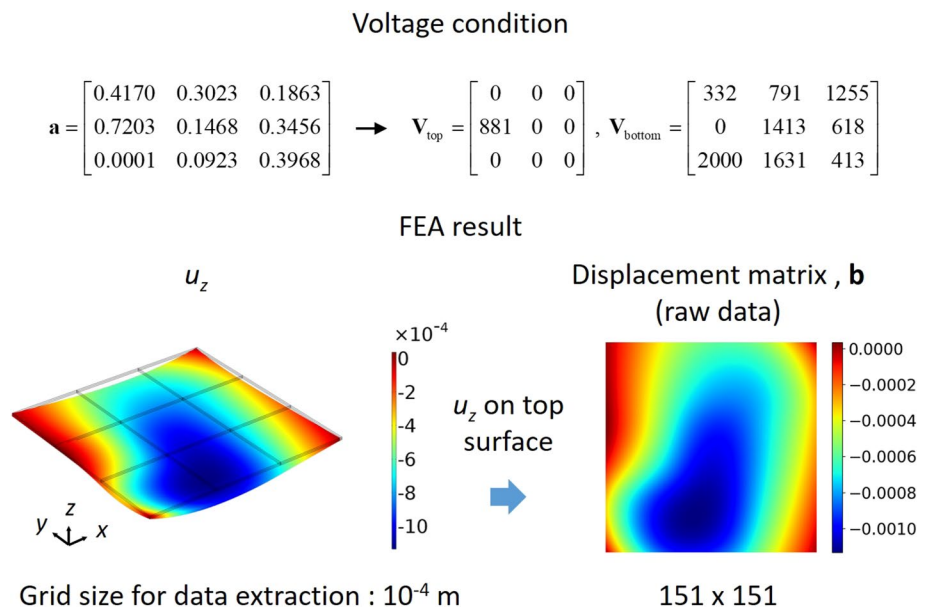
Figure 8 shows an example of electric potential matrices \mathbf{V}_{top} and $\mathbf{V}_{\text{bottom}}$ calculated by a randomly determined voltage condition matrix \mathbf{a} and the corresponding displacement field in z -direction. In this study, the z -direction displacement field on the top surface is considered as representative information on the deformation shape of the considered DEA. Thus, values of u_z are extracted with a grid size of 10^{-4} m on the top surface to define a displacement matrix \mathbf{b} of size 151×151 . After performing FEA under various voltage conditions, 4333 sets of the voltage condition matrix \mathbf{a} and the displacement matrix \mathbf{b} were generated. As a side note, there were cases where the nonlinear solver of the FEA could not find a solution and caused a trivial solution of 0. For this reason, the 4333 FEA data were obtained when the solution was normally found under 5000 voltage conditions.

Present study was conducted using a PC with Intel(R) Core(TM) i7-6700 CPU @ 3.40GHz and 16 GB RAM. The FEA for one data took approximately 100 s, and the time varies depending on the voltage condition.

Fig. 7 Setting of the electric potentials on the top and bottom surfaces

$$V_{\text{top}}^{i,j} = \text{round}(V_{\text{max}} \times \max(2a^{i,j} - 1, 0)) \quad V_{\text{bottom}}^{i,j} = \text{round}(V_{\text{max}} \times \max(-2a^{i,j} + 1, 0))$$

Fig. 8 Displacement matrix **b** generated from a randomly determined voltage condition matrix **a**



3.2 Data set for ANN construction

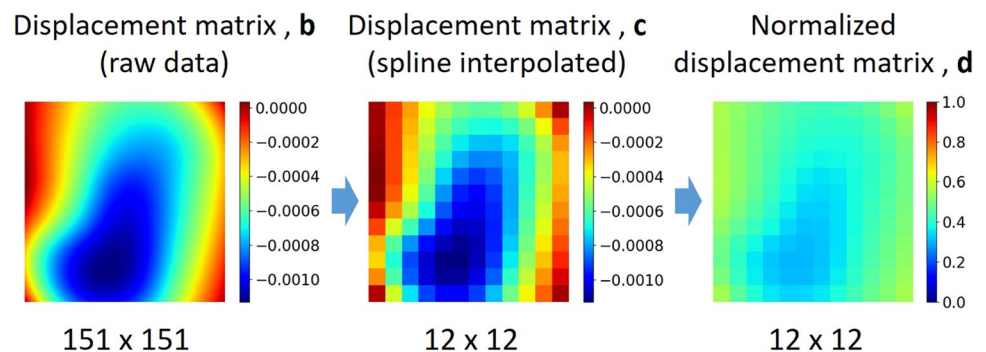
The displacement matrix **b** shown in Fig. 8 has a relatively large data size ($151 \times 151 = 22,801$) to be used in the early study of ANN construction for the DEA. If a displacement matrix of size 151×151 is used as an input of the ANN for inverse mapping, the front layers of the ANN are expected to include a role of lowering the resolution of high-dimensional data. Therefore, to increase the training efficiency of ANNs, displacement matrices with a reduced dimension in advance are used in the ANN training. Even if a displacement matrix of reduced-size is predicted by the ANN for forward mapping, a displacement matrix of size 151×151 can be obtained appropriately by increasing the resolution. Since ANNs typically take input values between 0 and 1 and produce output values between 0 and 1, the range of the element values is also unsuitable for ANN construction. For this reason, the generated 4333 displacement matrices **b** are preprocessed as shown in Fig. 9. First, the displacement matrix **b** is transformed into the displacement matrix **c** of size 12×12 by spline interpolation. In general, since the

size of matrices doubles or halves through ANN, the reduced size of the displacement matrix was set to be 4 times the size of the voltage condition matrix, 3×3 . Then, the elements of the displacement matrix **c** are normalized between 0 and 1 using Eq. (10). Here, $\alpha (= -0.002529)$ and $\beta (= 0.002054)$ are the minimum and maximum values among the all elements of the 4333 displacement matrices **c**, respectively. In other words, all data are normalized using the same minimum and maximum values. Finally, the normalized displacement matrix **d** of size 12×12 is generated. It is noted that both matrices **a** and **d** consist only of values between 0 and 1.

$$\mathbf{d} = \frac{\mathbf{c} - \alpha}{\beta - \alpha} \quad (10)$$

After the preprocess, 4333 sets of the voltage condition matrix **a** and the normalized displacement matrix **d** were prepared for ANN construction. In the case of predicting the displacement field, the voltage condition matrix **a** can be used as an input of the ANN, and the normalized displacement matrix **d** can be used as a correct answer of the output

Fig. 9 Preprocess for the displacement matrices **b**



of the ANN. Conversely, in the case of predicting the voltage condition, the normalized displacement matrix \mathbf{d} can be used as an input of the ANN, and the voltage condition matrix \mathbf{a} can be used as a correct answer of the output of the ANN. Of the total 4333 generated data, 3890 data, which are about 90 %, are used as a training data set to train the ANN. Other 216 data, which are about 5 %, are used as a validation data set to monitor the overfitting of the ANN to the training data set. The remaining 227 data are used as a test data set that are not used in the training process of ANN. Prior to ANN training, entire data set was divided into the training data set, validation data set, and test data set. The split data sets are used repeatedly to train and test both models. In other words, both models are trained with exactly the same data set. We just exchanged the input data and the correct answer data for two ANNs.

4 Prediction of displacement field

4.1 ANN for forward mapping

This section details the construction of the ANN for predicting the displacement field of the DEA from a specific voltage condition. In other words, the ANN that approximates the normalized displacement matrix \mathbf{d} from the voltage condition matrix \mathbf{a} is constructed in this section. In this study, the ANN construction was performed in the framework of Keras. Keras works with TensorFlow library and Python environment. The versions used in the study are Keras 2.2.4, TensorFlow 2.1.0, and Python 3.7.7. TensorFlow ran on CPU without using GPU.

Figure 10 shows the composition of the ANN for forward mapping that calculates the output matrix \mathbf{Y}_p from the input matrix \mathbf{X} . According to the basic guidelines for ANN construction, a set of voltage condition matrices \mathbf{a} of size 3×3 is used as the input matrix \mathbf{X} of size $n \times 3 \times 3 \times 1$, where n

is the number of data. Considering the corresponding correct answer matrix \mathbf{Y} consisting of normalized displacement matrices \mathbf{d} of size 12×12 , the size of the output matrix \mathbf{Y}_p should be $n \times 12 \times 12$. Here, the output matrix \mathbf{Y}_p means a set of predicted normalized displacement matrices \mathbf{d}_p of size 12×12 . The input matrix \mathbf{X} and the output matrix \mathbf{Y}_p can be regarded as a set of image data. Thus, the presented ANN consists of convolution layers and transposed convolution layers which are widely used matrix operations in image processing techniques (Krizhevsky et al. 2017). By using the convolution layer, the number of ANN parameters to be trained can be reduced. The transposed convolution layer serves to increase the number of image pixels within the ANN process. In the forward mapping, since the size of the output matrix is larger than the size of the input matrix, it is appropriate that the size of internal matrices through layers gradually increases. The transposed convolution plays this role. Both mathematical layers transform local image information using filters and then conduct a non-linear operation using the rectified linear unit (ReLU) activation function (Nair and Hinton 2010).

In the first and second convolution layers, the number of filters is set to 128 to generate a lot of intermediate images, so-called feature maps. Then, the number of filters is reduced by half, i.e., from 128 to 64 in the transposed convolution layer. After that, additional convolution layers and transposed convolution layer are applied in the same way. In the last convolution layer (indicated by C1 in Fig. 10), the number of filters is set to 1 to generate the 12×12 image data. Except for the last convolution layer, the size of filters is 3×3 . From our test, the last convolution layer with a filter size of 1×1 contributes to better prediction performance of the presented ANN. Regarding the strides of applying filters, the stride size of 1×1 of the convolution layers maintains the number of image pixels. On the other hand, the stride size of 2×2 of the transposed convolution layers doubles the number of image pixels in height and width, respectively.

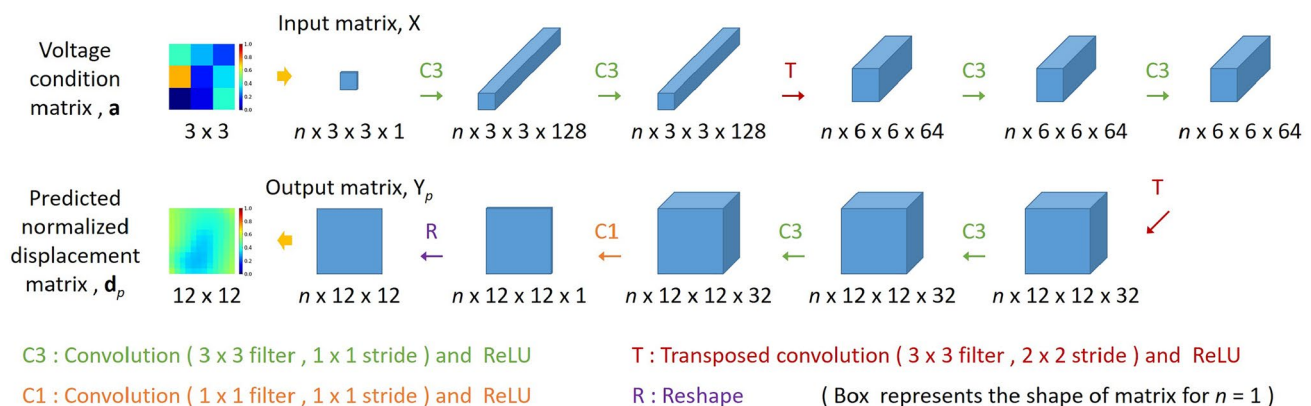


Fig. 10 Composition of the presented ANN for forward mapping

Regarding the padding techniques, so-called same padding is used to achieve the aforementioned points. The numbers of filters and layers were appropriately determined from the results with good prediction performance through trial and error and adjustment. In addition, numbers that cause excessive training time were excluded. The suggested numbers of filters and layers cannot be guaranteed to be optimal. However, further adjustments do not significantly change performance. Regarding the number and characteristics of the data covered in this study, excessively large or small numbers of filters and layers make the training of ANNs ineffective.

In the training process of the ANN, the optimization parameters, i.e., the filters and biases of the convolution layers and transposed convolution layers, are optimized for a loss function. The loss function is defined as the mean square error (MSE) between the predicted output matrix \mathbf{Y}_p and the corresponding correct answer matrix \mathbf{Y} . To evaluate the prediction performance of the ANN intuitively, the mean absolute error (MAE) is also observed during the training process. The optimization parameters are updated by the Adam algorithm using the gradients of the loss function for the optimization parameters (Kingma and Ba 2014). The initial values of the filters are set to a random normal distribution with a mean of 0 and a standard deviation of 0.1. The initial values of the biases are set to zero. A training data set is divided into batches and the optimization parameters are updated consecutively using each batch. A process in which all batches of the training data set are used once is called an epoch. The training process consists of many epochs enough to converge the loss function. Through trial and error, an appropriate batch size was determined to be 5. The learning rate representing the degree of parameter update was set to 0.0005. It is noted that the appropriate learning rate is affected by the batch size. The total training time of ANN took approximately 80 min for 1000 epochs, which is not a burdensome time.

Figure 11 shows the histories of MSE and MAE during the training process. The MSE and MAE at each epoch for the training data represent the means of the MSEs and MAEs obtained consecutively for all batches of the training data set, respectively. When the number of epochs reached 1000, the MSE values for both training and validation data were sufficiently converged. Because both MSE and MAE values for the validation data decreased gradually, overfitting on the training data was not seen. After completing the ANN training, the MSE and MAE were calculated for the training data set, validation data set, and test data set, respectively, as shown in Table 1. For the three types of data sets, MAEs are less than 0.006, which is considered an acceptable prediction error. The MAE for the test data set that is not directly or indirectly involved in the training process is also similar to the MAE for the validation data set.

4.2 Prediction results of displacement field

Using the ANN for forward mapping, the predicted normalized displacement matrix \mathbf{d}_p is obtained from the voltage condition matrix \mathbf{a} . Figure 12 represents all element values of the predicted normalized displacement matrices \mathbf{d}_p compared with the corresponding correct values. For the training data set, most of the predicted values are very close to the correct values. For the test data set, some predicted values are slightly different from the correct values, but most of the predicted values are still close to the correct values.

Table 1 The MSE and MAE for the three types of data sets after training the ANN for forward mapping

Data set	Training	Validation	Test
MSE	0.000007	0.000089	0.000131
MAE	0.001836	0.005138	0.005768

Fig. 11 Histories of MSE and MAE during the training process of the ANN for forward mapping

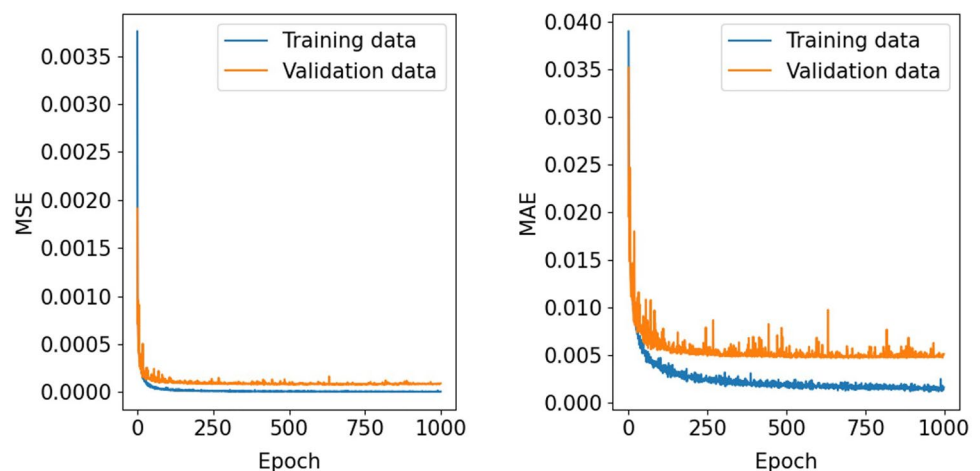
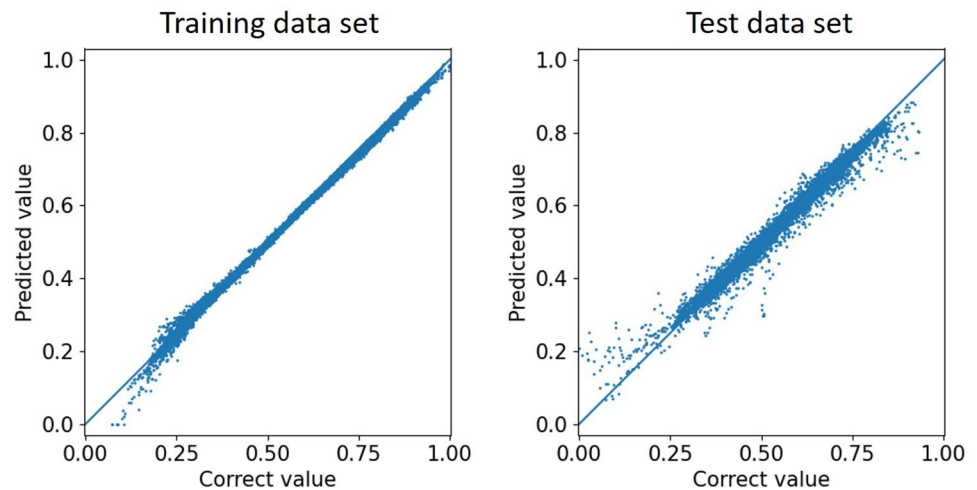


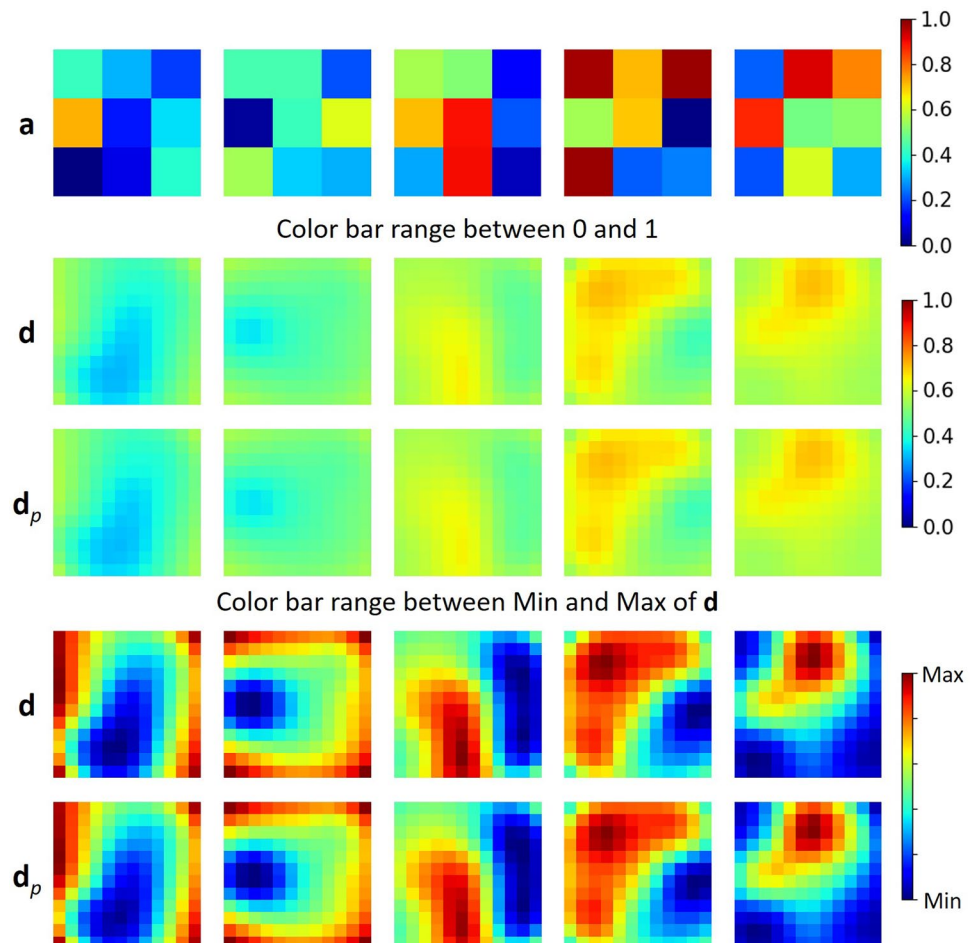
Fig. 12 Predicted values of normalized displacement matrices \mathbf{d}_p compared with the corresponding correct values



To intuitively judge the prediction accuracy, the image of the predicted normalized displacement matrix \mathbf{d}_p is compared with the image of the correct normalized displacement matrix \mathbf{d} . First, the prediction results by the voltage condition matrices \mathbf{a} of 5 training data are shown

in Fig. 13. To clarify the comparison, images with a color bar range between the minimum and maximum values of the correct normalized displacement matrix \mathbf{d} are also displayed. Comparing the images by colors, the predicted

Fig. 13 Prediction results for 5 training data using the ANN for forward mapping



normalized displacement matrix \mathbf{d}_p is very similar to the correct normalized displacement matrix \mathbf{d} .

Next, the prediction results by the voltage condition matrices \mathbf{a} of 5 test data are shown in Fig. 14. Looking closely at the colors of the images, a slight difference is found between the predicted normalized displacement matrix \mathbf{d}_p and the correct normalized displacement matrix \mathbf{d} . Nevertheless, the prediction performance of the ANN can be considered satisfactory.

As a further test, a user-defined voltage condition matrix \mathbf{a}_{user} was considered as shown in Fig. 15. The predicted normalized displacement matrix \mathbf{d}_p for the user-defined voltage condition matrix \mathbf{a}_{user} shows a significant agreement with the correct normalized displacement matrix \mathbf{d} . As a side note, the predicted displacement matrix \mathbf{c}_p can be additionally calculated using Eq. (11), which is derived from Eq. (10). Since the normalized displacement matrix \mathbf{d} is well predicted from the given voltage condition matrix \mathbf{a} , the present ANN is worth using as a surrogate model for the FEA.

$$\mathbf{c}_p = (\beta - \alpha)\mathbf{d}_p + \alpha \quad (11)$$

The presented ANN is a relatively small-scale network and has a shallow layer depth. Since the implementation of ANN is performed with limited computing capacity, constructing an ANN with large-scale and deeper layer depth can cause a burden on the computation time. From the perspective of effective utilization of ANN, an ANN that can be calculated in a short time is preferred. In addition to the computation time aspect, ANNs of relatively small size are advantageous in finding optimal ANN parameters using a small number of data.

As an additional content, we compared the performances of different activation functions regarding to the presented ANN composition in Fig. 10. Table 2 shows the MAEs of the trained ANN when using five different activation functions (LeakyReLU, ReLU, Swish, ELU, and Sigmoid). The MAE values for the five activation functions show similar levels. Comparing these functions based on the MAE on the test data, LeakyReLU performs best performance, followed by ReLU. However, considering the fluctuations and degree of convergence in performance according to the learning epoch, it is difficult to clearly judge the superiority of the activation functions by their performances at a particular

Fig. 14 Prediction results for 5 test data using the ANN for forward mapping

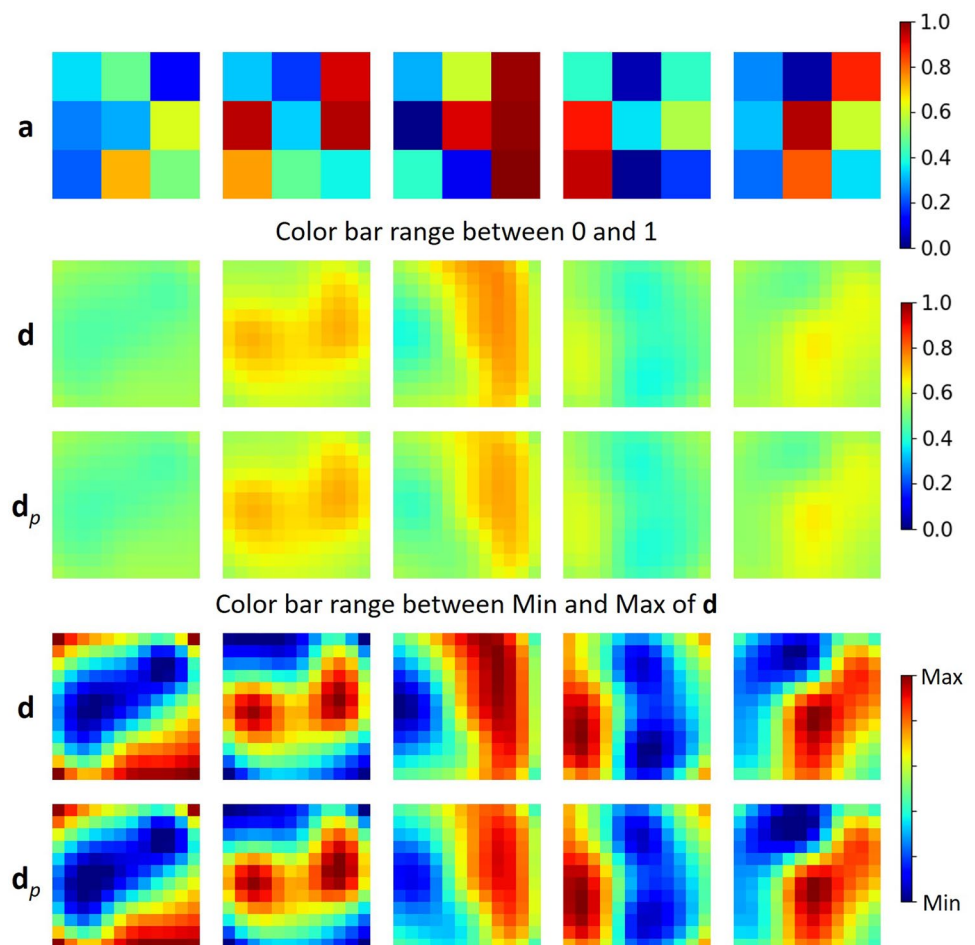


Fig. 15 Prediction result for the user-defined voltage condition matrix \mathbf{a}_{user}

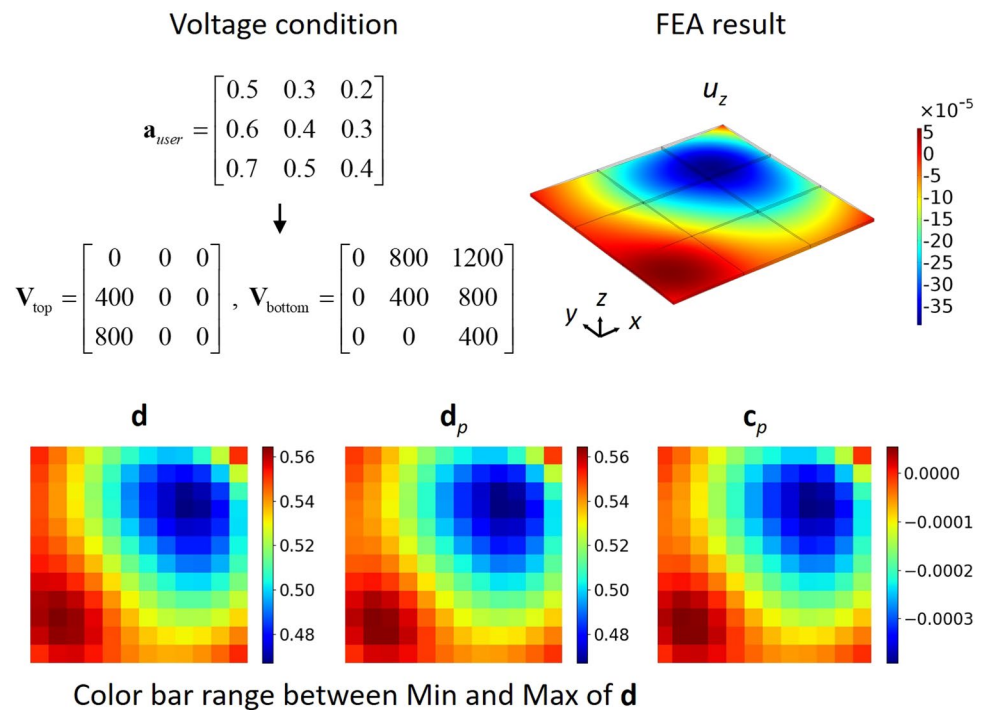


Table 2 Comparison of different activation functions in the ANN for forward mapping

Activation function	MAE(training)	MAE(validation)	MAE(test)
LeakyReLU	0.001585	0.004318	0.004904
ReLU	0.001836	0.005138	0.005768
Swish	0.001699	0.005293	0.006067
ELU	0.002322	0.005449	0.006162
Sigmoid	0.001619	0.005789	0.006500

epoch. In this study, the most commonly used ReLU was adopted.

In general, convolution layers are known to be more effective in ANN training than fully connected layers when the input of ANNs is an image. In this study, ANNs composed of fully connected layers were also attempted, but no advantage was found compared to the ANN composed of convolution layers. The performances of ANNs composed of fully connected layers are shown in Table 3. As an activation function, ReLU was used, and the other training parameters

are the same as those described in Sect. 4.1. The error values presented in Table 3 are all greater than those of ANN composed of convolution layers in Table 1. If the size of fully connect layers is too large or the number of layers increases, training of ANNs may become rather difficult.

5 Determination of voltage condition: Approach 1

5.1 GA for inverse problem

Compared with the FEA, the ANN can calculate a predicted normalized displacement matrix \mathbf{d}_p instantaneously. The time required to predict one data was measured as 0.15 s, which can be seen as almost a real-time response. Predictions based on the ANN are computationally efficient compared to the FEA simulation, which consumes approximately 100 s. Therefore, when trying to find a voltage condition that implements a specific displacement field, the ANN can be utilized to explore a very large number of voltage conditions.

Table 3 Performances of ANN for forward mapping composed of fully connected layers

Layer numbers	Neurons per layer	MAE(training)	MAE(validation)	MAE(test)
3 hidden layers	12x12x1	0.006645	0.010496	0.011318
3 hidden layers	12x12x4	0.002295	0.005734	0.006605
4 hidden layers	12x12x4	0.002466	0.006127	0.006757
6 hidden layers	12x12x4	0.003071	0.007078	0.007939
3 hidden layers	12x12x8	0.002588	0.006007	0.006769

This section uses the ANN to determine the voltage condition matrix \mathbf{a} that provides the predicted normalized displacement matrix \mathbf{d}_p most similar to the target normalized displacement matrix \mathbf{d}_t . As a search method to determine the voltage condition matrix \mathbf{a} , a GA is used for its simplicity. The design variables of the optimization problem to be solved by GA are the elements of the voltage condition matrix \mathbf{a} . The objective function f to be minimized is set to the MAE between the target normalized displacement matrix \mathbf{d}_t and the predicted normalized displacement matrix \mathbf{d}_p as defined in Eq. (12).

$$f(\mathbf{a}) = \text{mean}(\text{abs}(\mathbf{d}_t - \mathbf{d}_p(\mathbf{a}))) \quad (12)$$

Figure 16 shows the schematic diagram of the GA used. As an initial population of the first generation, 1000 random individuals are produced. The variables of each individual are expressed by the elements of the voltage condition matrix \mathbf{a} . After calculating the objective function f of each individual, 300 parent individuals are selected. Among the 300 individuals, 10 individuals are selected by the elitism, i.e., the highest order of the objective function value. The remaining 290 individuals are selected by the roulette wheel selection method which uses the selection probability according to the objective function value. By using the 300 parent individuals, 700 child individuals are produced by

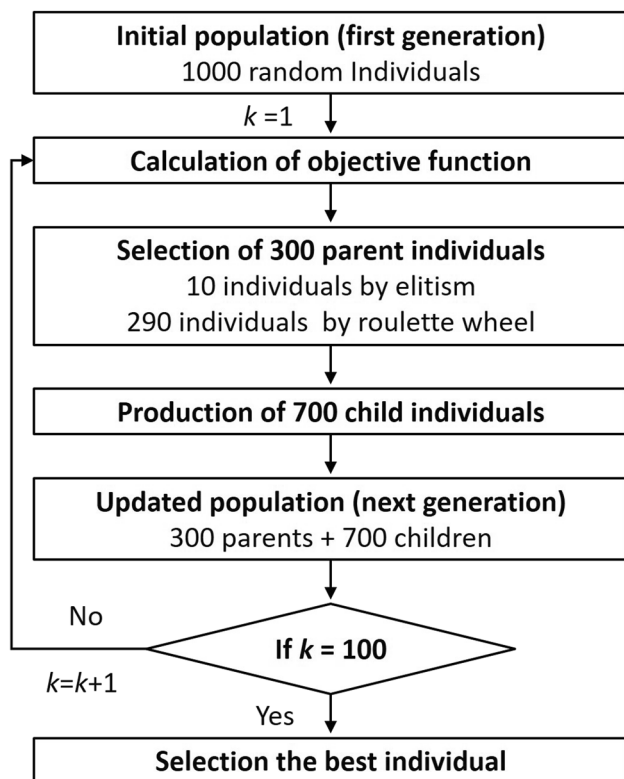


Fig. 16 Schematic diagram of the GA used

uniform crossover and mutation as shown in Fig. 17. The mutation occurs for each variable of individuals with a probability of 0.1. Then, the 300 parent individuals and the 700 child individuals become the updated population of the next generation. After 100 iterations of the population update, the best individual with the lowest objective function value is finally selected.

GA results depend on the GA parameters and random trials. Therefore, we tested the parameter values in several examples and derived commonly valid values in the examples. Although it is most desirable to obtain optimal results by setting different GA parameters for each problem and performing multiple random trials, we applied the GA to each problem using the same parameter values and random number seed. In order to show the general performance of the GA, the results obtained in this way are presented as representatives. The time taken to run the GA for the selected conditions was approximately 35 min. Increasing the size of population and the number of iterations may improve the performance of GA, but it may lead to excessive time consumption depending on the purpose.

5.2 Examples of voltage condition determination: Approach 1

Some examples are provided to demonstrate the effectiveness of the voltage condition determination method using the ANN-based prediction and the GA. Figure 18 illustrates the determination of voltage condition using the test data (corresponding to the first data used in Fig. 14). Here, the normalized displacement matrix \mathbf{d} of the test data is regarded as the target normalized displacement matrix \mathbf{d}_t . Also, the

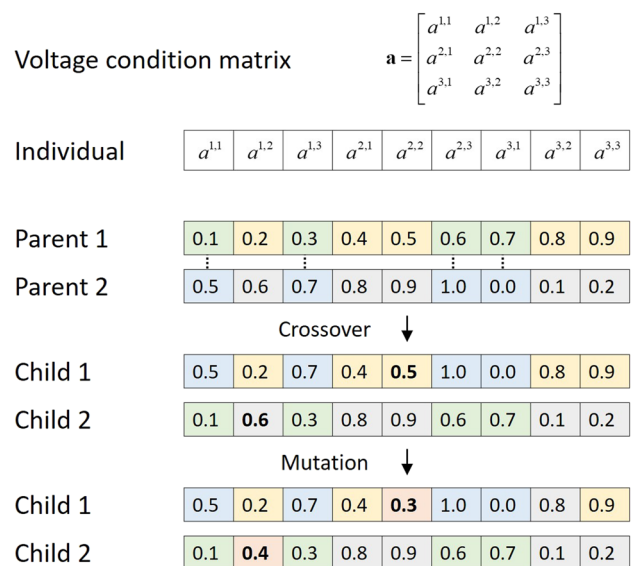
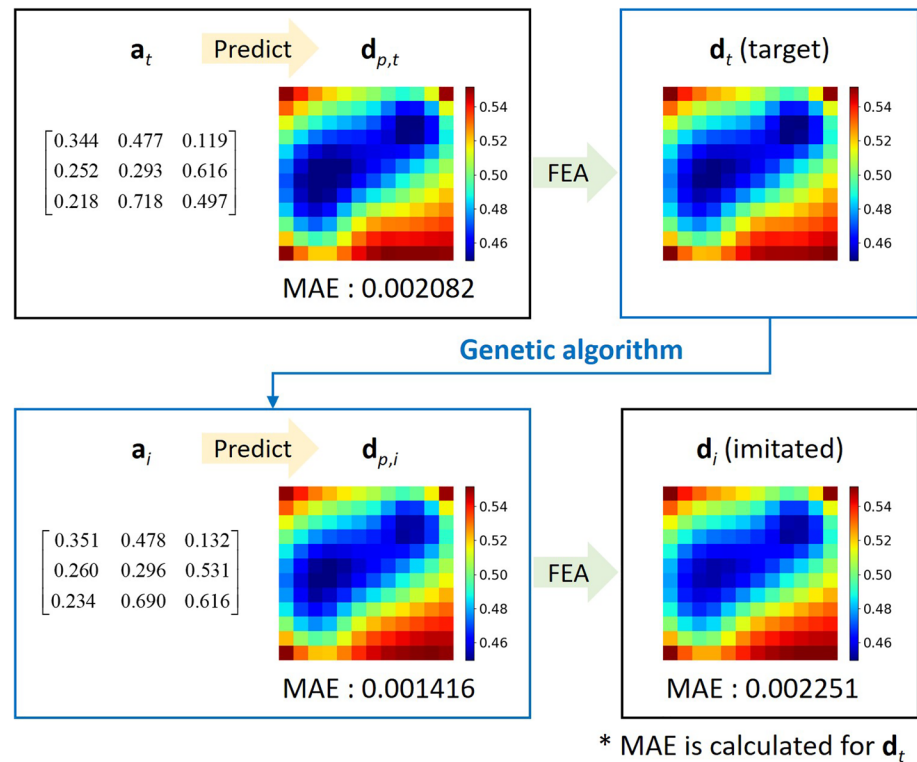


Fig. 17 Crossover and mutation of the GA used

Fig. 18 Determination of voltage condition using the GA for the target normalized displacement matrix \mathbf{d}_t from the test data



voltage condition matrix \mathbf{a} of the test data is considered as the unknown target voltage condition matrix \mathbf{a}_t that should be determined. Then, using the GA described above, the imitated voltage condition matrix \mathbf{a}_i was determined. Looking at the result, the elements of the imitated voltage condition matrix \mathbf{a}_i represent similar values to those of the target voltage condition matrix \mathbf{a}_t . The predicted normalized displacement matrix $\mathbf{d}_{p,i}$ for the imitated voltage condition matrix \mathbf{a}_i also represents an acceptable MAE of 0.001416 compared with the target normalized displacement matrix \mathbf{d}_t . This MAE value is smaller than the MAE value ($=0.002082$) of the predicted normalized displacement matrix $\mathbf{d}_{p,t}$ for the target voltage condition matrix \mathbf{a}_t . Since the search by GA is performed based on the predicted values, a MAE value lower than 0.001416 is not significant. After that, FEA was performed on the imitated voltage condition matrix \mathbf{a}_i to obtain an imitated normalized displacement matrix \mathbf{d}_i . Visually, the imitated normalized displacement matrix \mathbf{d}_i does not look much different from the target normalized displacement matrix \mathbf{d}_t . The MAE is also represents an acceptable value of 0.002251.

The previous example of Fig. 18 is the case that the target normalized displacement matrix \mathbf{d}_t was actually obtained through FEA from the already known target voltage condition matrix \mathbf{a}_t . However, the presented voltage condition determination method can be recognized as useful when it is not known whether the target normalized displacement matrix \mathbf{d}_t can be obtained through FEA. Therefore, in order

to confirm the usefulness of the presented method, the target normalized displacement matrix \mathbf{d}_t of Fig. 18 was arbitrarily modified as shown in Fig. 19. Here, the modification was made so that the values of the center region were slightly increased. In other words, the target normalized displacement matrix \mathbf{d}_t of Fig. 19 was not obtained directly through FEA, and the corresponding target voltage condition matrix \mathbf{a}_t is unknown. Then, an imitated voltage condition matrix \mathbf{a}_i was obtained in the same way, and the corresponding predicted normalized displacement matrix $\mathbf{d}_{p,i}$ represented a MAE of 0.002263. This MAE value is somewhat larger than the corresponding MAE value ($=0.001416$) in the previous example. Subsequently, an imitated normalized displacement matrix \mathbf{d}_i was obtained by FEA, which represented a MAE of 0.002785. This MAE value is slightly larger than the corresponding MAE value ($=0.002251$) in the previous example, but to a similar extent. Considering that the target normalized displacement matrix \mathbf{d}_t may not be accurately obtained by FEA, such an increase in the MAE value can be considered reasonable. Visually, the imitated normalized displacement matrix \mathbf{d}_i shows a somewhat similar pattern compared with the target normalized displacement matrix \mathbf{d}_t .

Figure 20 represents the objective function value of the best individual in the GA processes of the previous examples. It can be seen that the objective function value continues to decrease as the population update progresses. When the number of updates approaches 100, the objective function value hardly decreases.

Fig. 19 Determination of voltage condition using the GA for the target normalized displacement matrix \mathbf{d}_t from the modified test data

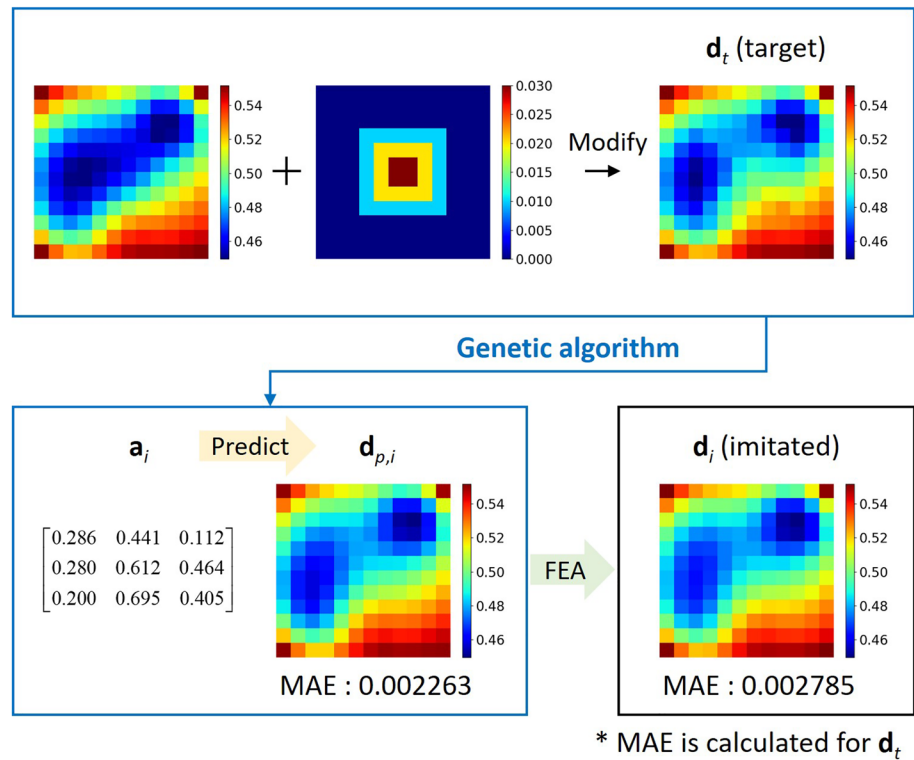
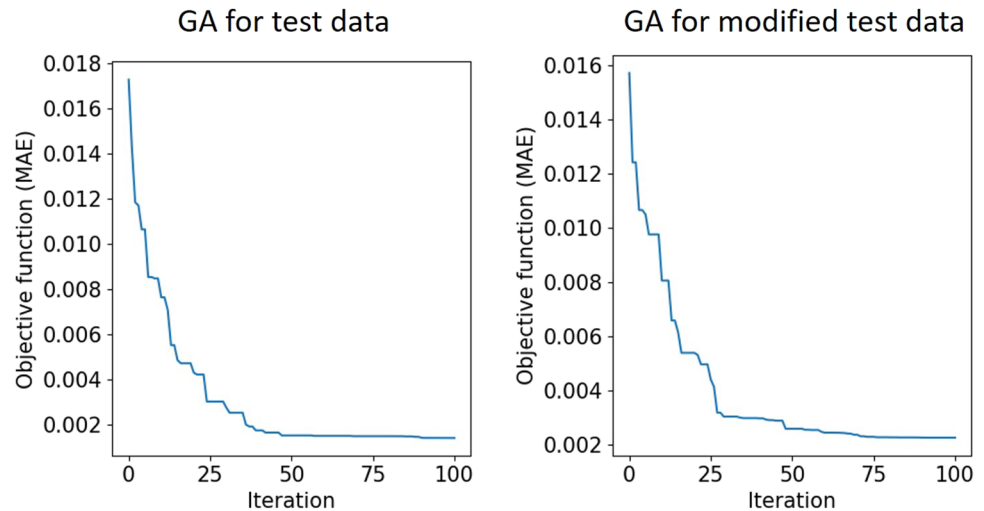


Fig. 20 Graphs for the objective function value of the best individual during the GA processes of Figs. 18 and 19



In the next example, five user-defined target normalized displacement matrices \mathbf{d}_t are considered. As shown in the first column of Fig. 21, simple image patterns that can be easily thought of are used for the target normalized displacement matrix \mathbf{d}_t . In fact, it can be known intuitively that it is difficult to obtain these simple image patterns of displacement field with considerable accuracy through the FEA. Therefore, it is aimed to search the voltage condition that provides the most similar image pattern of displacement field as possible. In the results of Fig. 21, the MAE values of the predicted normalized displacement matrices $\mathbf{d}_{p,i}$ are

much larger than the corresponding MAE values in the previous two examples of Figs. 18 and 19. This fact implies that the target normalized displacement matrices \mathbf{d}_t considered here are difficult to be approximately implemented through the FEA. FEA was performed using the imitated voltage condition matrix \mathbf{a}_i obtained by GA. The resultant DEA shape colored by the z -direction displacement u_z from the FEA is shown in Fig. 21 (denoted by $\text{FEA}(u_z)$). As in the previous two examples, the MAE of the imitated normalized displacement matrix \mathbf{d}_i is greater than the MAE of the predicted normalized displacement matrix $\mathbf{d}_{p,i}$, except for the

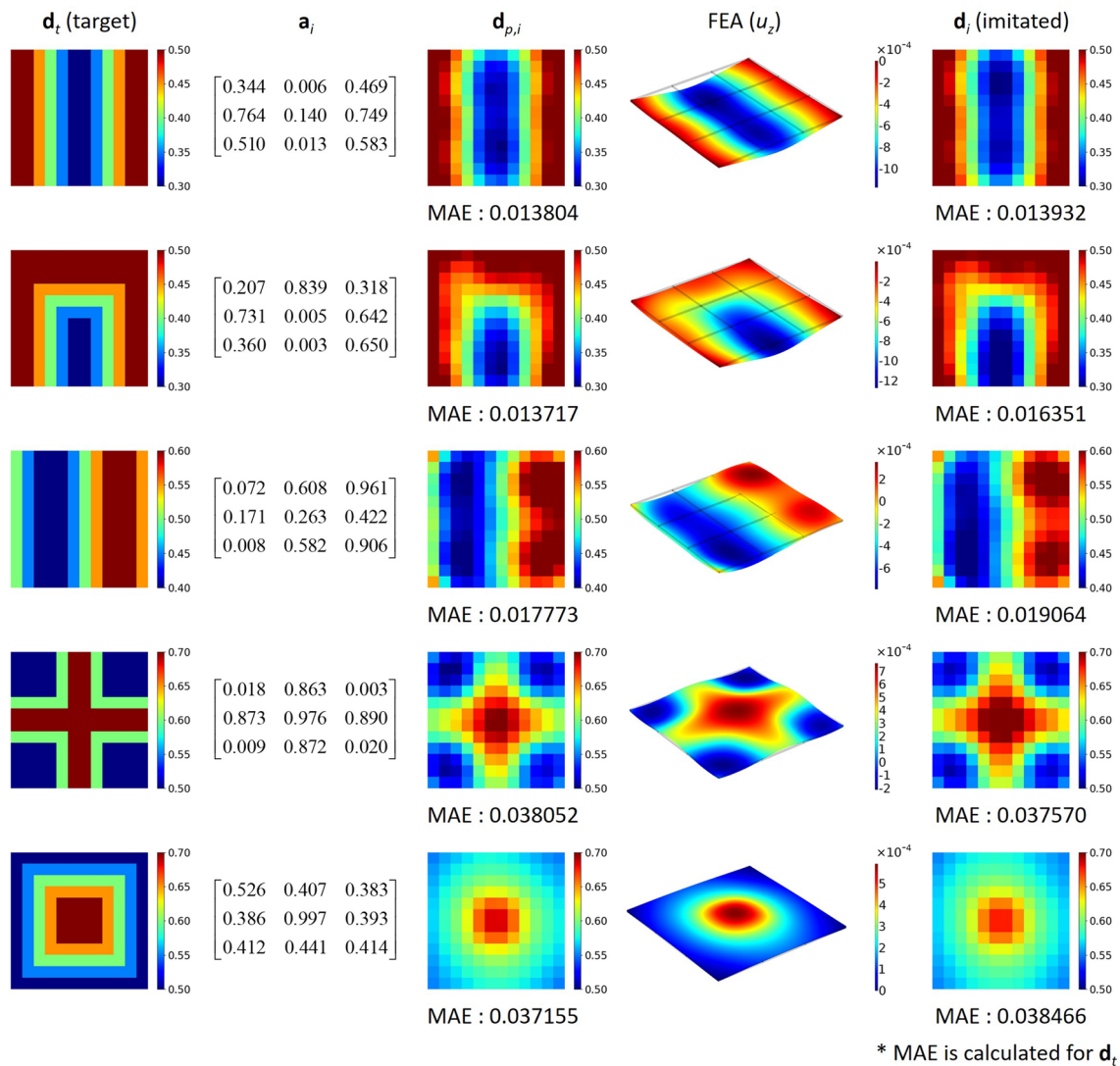


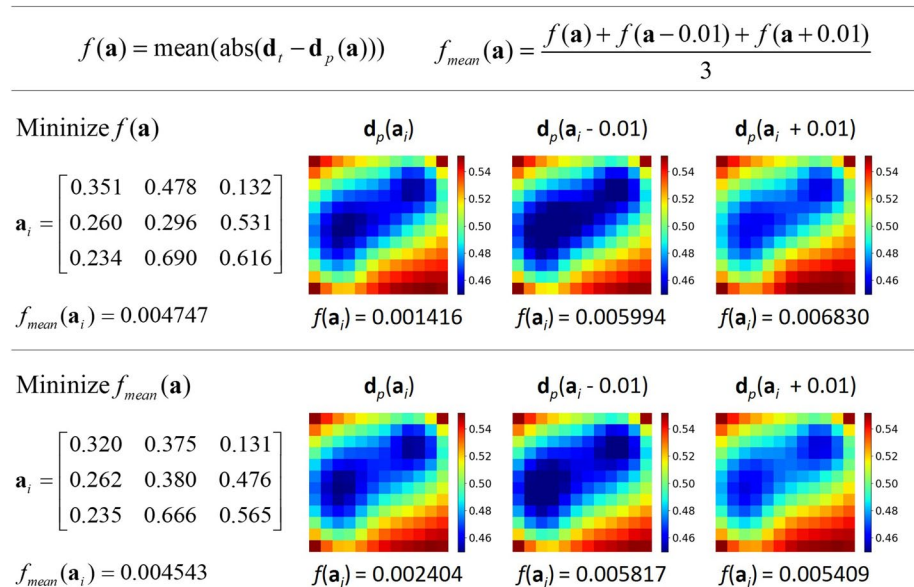
Fig. 21 Determination of voltage condition using the GA for the user-defined target normalized displacement matrix \mathbf{d}_t

fourth case. Visually, the imitated normalized displacement matrix \mathbf{d}_i shows well the main features of the target normalized displacement matrix \mathbf{d}_t in all five cases. Meanwhile, the effect of changing the values of GA parameters was not large enough to significantly change the results. From the three examples presented, we judge that it is possible to appropriately determine the voltage condition of the DEA for the target displacement field without using time-consuming FEA.

As a further investigation, we considered uncertainty of voltage condition. First, the imitated voltage condition matrix \mathbf{a}_i obtained by GA in Fig. 18 was varied to small amount by subtracting or adding 0.01 to all elements of the matrix. Then, the predicted normalized displacement matrix $\mathbf{d}_{p,i}$ and the corresponding MAE to the target normalized displacement matrix \mathbf{d}_t was calculated as shown in Fig. 22. Due to the small variation of voltage

condition, the magnitude of the predicted normalized displacements decreased or increased as a whole. Since the pattern of the predicted displacement image has not changed significantly, it is judged that the influence of uncertainty of the voltage condition is not significant. As part of reducing the influence of uncertainty, we simply set the objective function of GA as a mean MAE for adjacent three voltage conditions, described as $f_{mean}(\mathbf{a})$ in Fig. 22. As a result of GA considering the mean MAE, the MAE ($=0.002404$) for the voltage condition as a solution is larger than the MAE ($=0.001416$) in the GA result considering a single MAE in the objective function. Instead, the MAEs for the two adjacent voltage conditions are smaller than those in the GA result considering a single MAE. The mean MAE for adjacent three voltage conditions $f_{mean}(\mathbf{a})$ is also smaller than that in the single-MAE based GA,

Fig. 22 Determination of voltage condition using the GA considering variations in voltage condition



which is a reasonable result according to the objective function setting.

6 Determination of voltage condition: Approach 2

6.1 ANN for inverse mapping

In this section, we attempt to directly determine the voltage condition for a target displacement field through the ANN for inverse mapping. Thus, the input data of the ANN for inverse mapping are a set of normalized displacement matrices \mathbf{d} , and the correct answer data are a set of voltage condition matrices \mathbf{a} . Figure 23 shows the composition of the ANN for inverse mapping to obtain the predicted voltage condition matrix \mathbf{a}_p .

The ANN for inverse mapping in Fig. 23 has an overall similar configuration to the previously constructed ANN for forward mapping in Fig. 10. To induce the the output matrix \mathbf{Y}_p of size $n \times 3 \times 3$ from the input matrix \mathbf{X} of size $n \times 12 \times 12 \times 1$, max pooling layers are used instead of the transposed convolution layers. The max pooling layer serves to halve the number of image pixels by taking the maximum value within the 2×2 element pool. In the inverse mapping, since the size of the output matrix is smaller than the size of the input matrix, it is appropriate that the size of internal matrices through layers gradually decreases. The max pooling plays this role. The number of filters in each convolution layer was slightly adjusted from the settings of the ANN for forward mapping. One thing to note is that the sigmoid function is used instead of the ReLU activation function in the last convolution layer. The reason for adopting the sigmoid function is to ensure

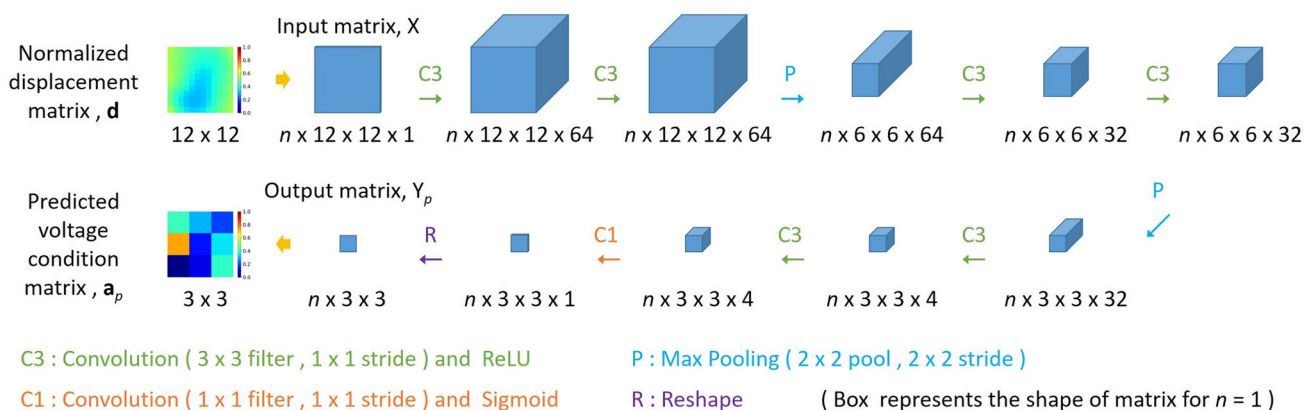


Fig. 23 Composition of the presented ANN for inverse mapping

Fig. 24 Histories of MSE and MAE during the training process of the ANN for inverse mapping

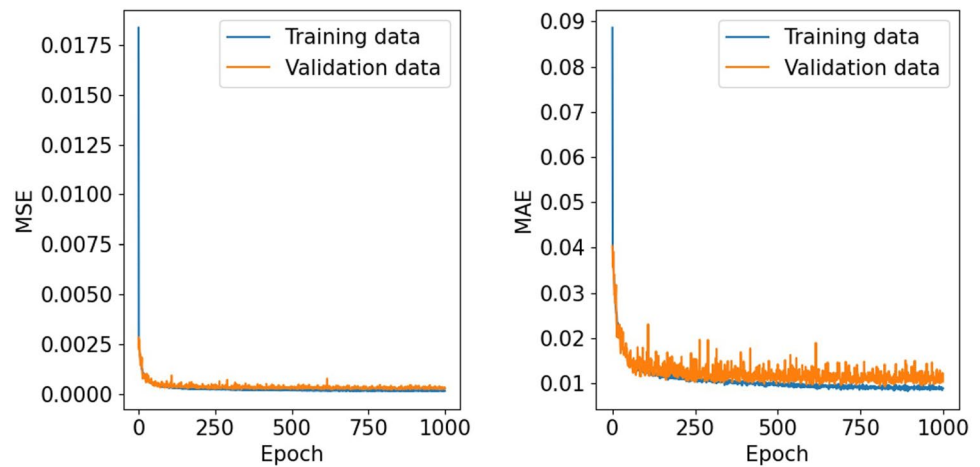


Table 4 The MSE and MAE for the three types of data sets after training the ANN for inverse mapping

Data set	Training	Validation	Test
MSE	0.000125	0.000268	0.000275
MAE	0.008107	0.010313	0.010337

that the element values of the predicted voltage condition matrix \mathbf{a}_p do not exceed 1. Of course, in the case of using the ReLU, if an element value greater than 1 occurs, it may be substituted with 1. The settings for the training of the ANN for inverse mapping are the same as those of the ANN for forward mapping, except the learning rate of 0.002.

Figure 24 shows the histories of MSE and MAE during the training process. After completing the ANN training, the MSE and MAE were calculated for the training data set, validation data set, and test data set, respectively, as shown in Table 4. Compared with the errors of the ANN

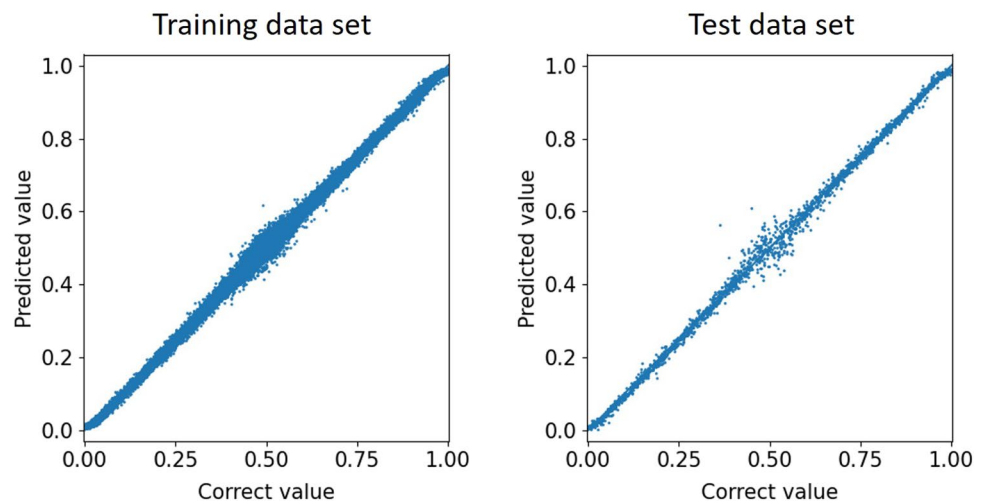
for forward mapping, the errors of the ANN for inverse mapping are larger, but within the acceptable range.

Using the ANN for inverse mapping, the predicted voltage condition matrix \mathbf{a}_p is obtained from the normalized displacement matrix \mathbf{d} . Figure 25 represents all element values of the predicted voltage condition matrices \mathbf{a}_p compared with the corresponding correct values. In both results for the training and test data sets, most of the predicted values are close to the correct values. The prediction results by the normalized displacement matrices \mathbf{d} of 5 test data are shown in Fig. 26. As well as the image representation, the element values of the predicted voltage condition matrix \mathbf{a}_p are similar to those of the correct voltage condition matrix \mathbf{a} .

6.2 Examples of voltage condition determination: Approach 2

The previous examples in Sect. 5.2 are addressed again to judge the feasibility of directly determining the voltage condition using the ANN for inverse mapping. Figure 27 shows

Fig. 25 Predicted values of voltage condition matrices \mathbf{a}_p compared with the corresponding correct values



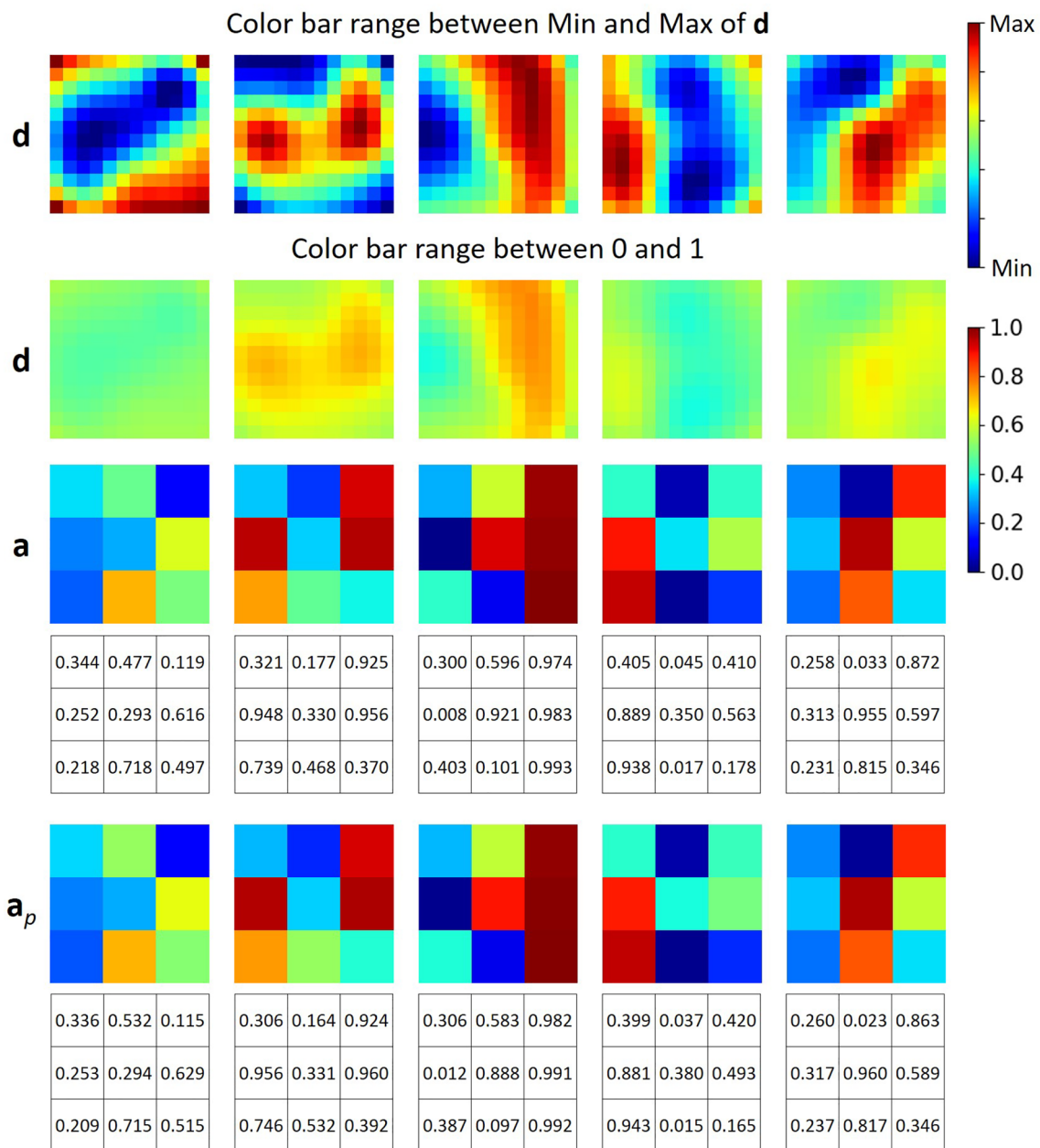


Fig. 26 Prediction results for 5 test data using the ANN for inverse mapping

the determination of voltage condition using the test data and its modification, where the considered target normalized displacement matrices \mathbf{d}_i are the same as in Figs. 18 and 19. In the result using the test data, the elements of the predicted voltage condition matrix $\mathbf{a}_{p,i}$ (named the same as the imitated voltage condition matrix \mathbf{a}_i) represent similar values to those of the target voltage condition matrix \mathbf{a}_i , presented in Fig. 18. This point has already been confirmed in first column of Fig. 26. The imitated normalized displacement matrix \mathbf{d}_i obtained by FEA represents a very low MAE of 0.000756. This value is lower than the corresponding value

(=0.002251) in Fig. 18, which is performed by the GA and ANN for forward mapping. This result implies that the ANN for inverse mapping may better predict the voltage condition when the target displacement field is likely to be approximately obtained by FEA.

In the result using the modified test data, however, the imitated normalized displacement matrix \mathbf{d}_i represents a MAE of 0.007458, which is larger than the corresponding value (=0.002785) in Fig. 19. When the imitated normalized displacement matrix \mathbf{d}_i is visually seen without matching the color bar range to the target normalized displacement

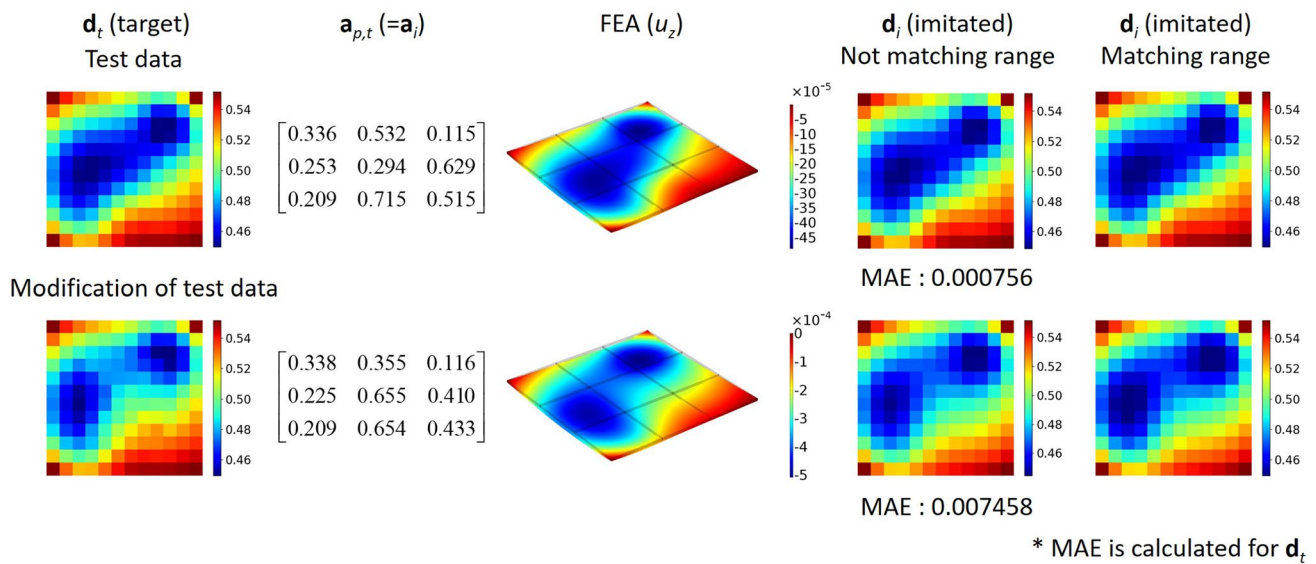


Fig. 27 Determination of voltage condition using the ANN for inverse mapping for the target normalized displacement matrix \mathbf{d}_t from the test data and its modification

matrix \mathbf{d}_i , the pattern and intensity by color are somewhat similar to those of the target normalized displacement matrices \mathbf{d}_t . But, matching the color bar range, the color intensity is increased and some discrepancies are visually revealed. This result implies that the ANN for inverse mapping may have shortcomings in predicting the voltage condition when the target displacement field is unlikely to be approximately obtained by FEA.

Then, the direct determination of voltage condition using the ANN for inverse mapping was tested for the user-defined target normalized displacement matrices \mathbf{d}_t as shown in Fig. 28. The same image patterns as in Fig. 21 are used as the target normalized displacement matrix \mathbf{d}_t . In the result, the images of the imitated normalized displacement matrices \mathbf{d}_i in the five cases roughly show the main features of the images of the target normalized displacement matrices \mathbf{d}_t . However, the MAE to the target in each case is much higher than the corresponding MAE in Fig. 21. This increase in the MAE is clearly visible when the color bar range is matched to that of the target normalized displacement matrix \mathbf{d}_t .

Comparing the results in Figs. 21 and 28, it is judged that the first approach in Sect. 5 (using GA and ANN for forward mapping) is more effective than the second approach in this section (using ANN for inverse mapping) for an arbitrary user-defined displacement field. The disadvantage of using the ANN for inverse mapping is understandable in that it is difficult to generalize the prediction performance of voltage condition even to the deformation that is difficult to be implemented in practice by DEA. To summarize the above, if the possibility of realization for the target displacement field is expected to be high, it is recommended to use the

ANN for inverse mapping from the viewpoint of real-time prediction ability. Otherwise, it is desirable to utilize search techniques based on the ANN for forward mapping, even though the search process takes several minutes.

7 Consideration of noise in training data

In this section, we investigate the effect of noise in the training data of ANN. The noise only applies to the training data for normalized displacement matrices \mathbf{d} . First, the ANN for forward mapping was constructed again by applying noise to the correct answer matrices \mathbf{Y} representing displacement fields. The conditions for training are the same as in the Sect. 4.1. The noise is randomly generated by standard normal distribution with the mean of 0 and the standard deviation of 0.01. The value of the standard deviation was selected appropriately to the extent that maintains the characteristics of the displacement field. Even after applying noise, the range of the training data is limited to be between 0 and 1. It is noted that overfitting phenomenon is observed during the training process when using the validation data without noise. In other words, trends of MSE and MAE for the validation data gradually increase again after a number of epochs. Accordingly, the number of epochs was limited to 100.

Table 5 shows the MSE and MAE values calculated by the ANN for forward mapping trained with noise. The three data sets used for calculation do not include noise in the correct answer matrices \mathbf{Y} . All the error values are larger than

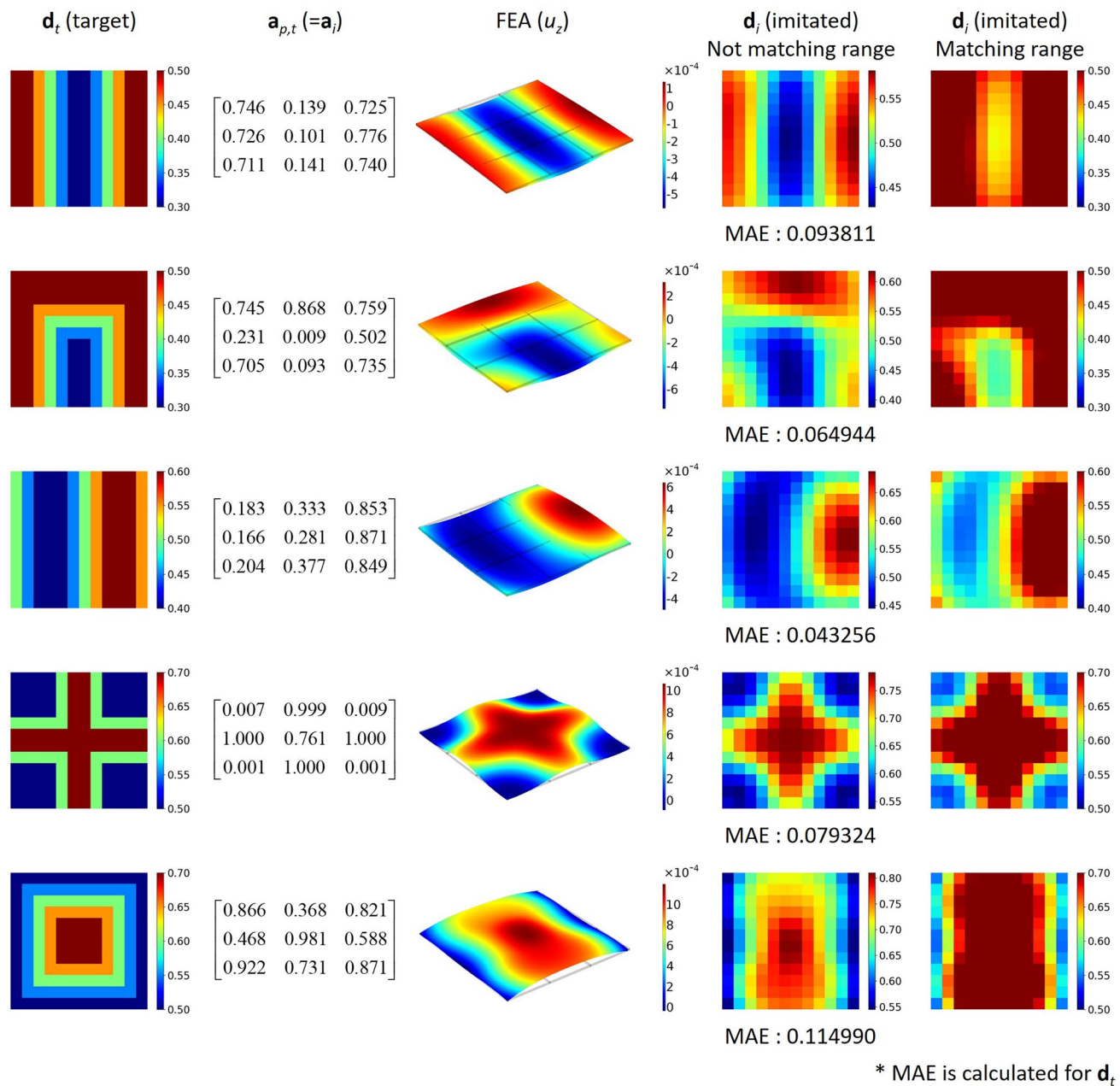


Fig. 28 Determination of voltage condition using the ANN for inverse mapping for the user-defined target normalized displacement matrix \mathbf{d}_t

the values in Table 1 obtained by the ANN trained without noise, but are within an acceptable range.

Images of the predicted normalized displacement matrices \mathbf{d}_p are provided in Fig. 29 for both training and test data. The images for the correct normalized displacement matrices \mathbf{d} with random noise are also shown for the training data. Even though the ANN was trained with the correct answer matrices \mathbf{Y} containing noise, the images for the predicted normalized displacement matrices \mathbf{d}_p do not show any noise-like features. Compared with the results in Figs. 13 and 14, the ANN trained with noise still shows

Table 5 The MSE and MAE for the three types of data sets after training the ANN for forward mapping with the training data including noise

Data set	Training	Validation	Test
MSE	0.000026	0.000116	0.000156
MAE	0.003909	0.006438	0.006860

Fig. 29 Prediction results for training and test data using the ANN for forward mapping trained with noise

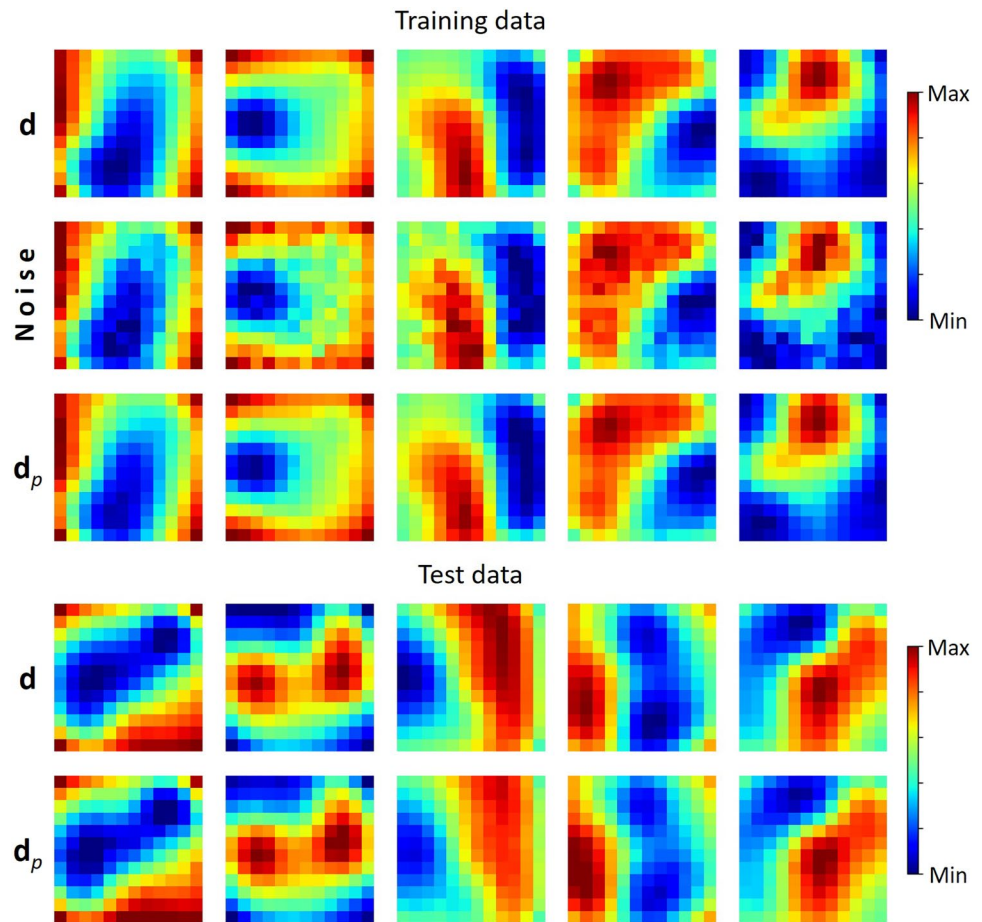


Table 6 The MSE and MAE for the three types of data sets after training the ANN for inverse mapping with the training data including noise

Data set	Training	Validation	Test
MSE	0.001354	0.001641	0.001699
MAE	0.025976	0.028219	0.027918

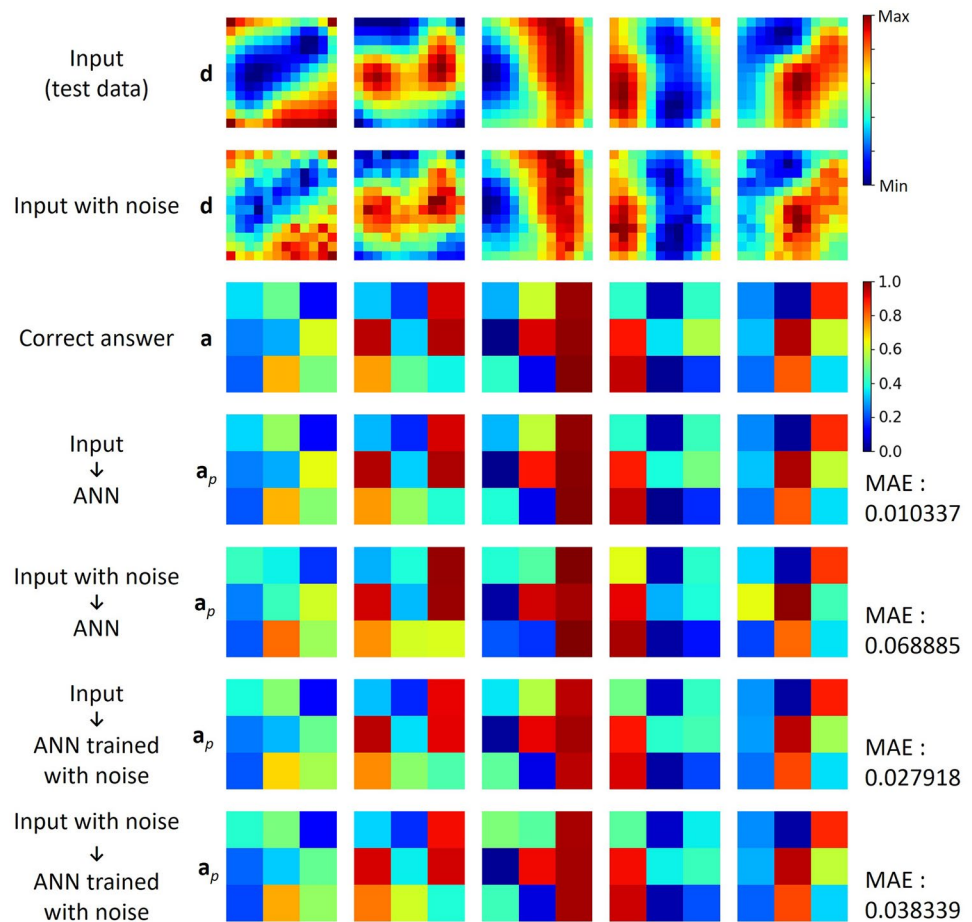
appropriate prediction performance. From this results, it can be inferred that ANN can be trained even with experimental data containing noise.

Next, the ANN for inverse mapping was constructed again by applying noise to the input matrices \mathbf{X} representing displacement fields. The conditions for training are the same as in the Sect. 6.1. Table 6 shows the MSE and MAE values calculated by the ANN for inverse mapping trained with noise. The three data sets used for calculation do not include noise in the input matrices \mathbf{X} . All the error values are larger than the values in Table 4 obtained with the ANN trained without noise. The MAE on the test data set is more than double compared with the corresponding MAE in Table 4.

Additionally, we checked the prediction results using the normalized displacement matrix \mathbf{d} containing noise as input to the ANN. The top two rows of Fig. 30 show the normalized displacement matrices \mathbf{d} of 5 test data with and without noise. Predicting the voltage condition matrix \mathbf{a} can be performed by both ANNs trained with and without noise. Accordingly, four cases need to be compared as shown in the bottom four rows of Fig. 30. When the input with noise was passed through the ANN trained without noise (as predicted in the 5th row), MAE for the entire test data has increased considerably (MAE: 0.068885). However, when the input with noise was passed through the ANN trained with noise (as predicted in the last row), the increase in MAE could be prevented to some extent (MAE: 0.038339).

With the ANN for inverse mapping trained with noise-containing data, the previous examples in Figs. 27 and 28 were performed again. The corresponding results are shown in Fig. 31, which shows the predicted voltage condition matrices $\mathbf{a}_{p,t}$ and the corresponding imitated normalized displacement matrices \mathbf{d}_t obtained by FEA for the target normalized displacement matrices \mathbf{d}_t . Comparing the results by the ANN trained with noise (shown in Fig. 31) with the results by the ANN trained without noise

Fig. 30 Prediction results for 5 test data (with/without noise) using the ANN for inverse mapping (trained with/without noise)



(shown in Figs. 27 and 28), we found an important fact. Paying attention to the MAE of the imitated normalized displacement matrix \mathbf{d}_i , the presented MAEs in Fig. 31 are lower than the MAEs shown in Figs. 27 and 28 except for the MAE for the test data (the first row in Fig. 31). Looking at the images of the imitated normalized displacement matrices \mathbf{d}_i with matched ranges, noticeable improvements in similarity to the target images are observed. In other words, the ANN trained with noise was effective in predicting the voltage condition for an arbitrary displacement field that can not be exactly obtained through FEA. This is because we prevented overfitting to the training data set containing noise by monitoring the prediction accuracy on the validation data set that does not contain noise. Even with training data set that does not contain noise, reducing training epochs may improve prediction performance on the non-FEA-based data to some extent, while decreasing prediction performance on the accurate FEA-based data. Since user-defined displacement data are not included in the training data set, the approach of directly mapping the inverse problem of this study has some limitations.

8 Conclusions

In this study, the applicability of an ANN-based surrogate model was investigated in determining the voltage condition to implement the deformation of DEA desired by a user. For this purpose, the present work was conducted based on FEA, excluding detailed theories and experimental implementations. In the inverse problem of a simple bilayer DEA with different voltages in each of the 3×3 divided regions, we utilized an ANN of moderate complexity. Even though large-scale ANN models and vast amounts of data were not used, it was possible to construct the ANNs with reliable prediction performance. As a solution to the inverse problem, we examined two approaches with opposite concepts. The first approach was to replace time-consuming FEA with an ANN-based surrogate model capable of immediate computation and use search techniques such as GA. The second approach was to construct an ANN-based prediction model that directly provides an answer to the inverse problem. Both approaches found well

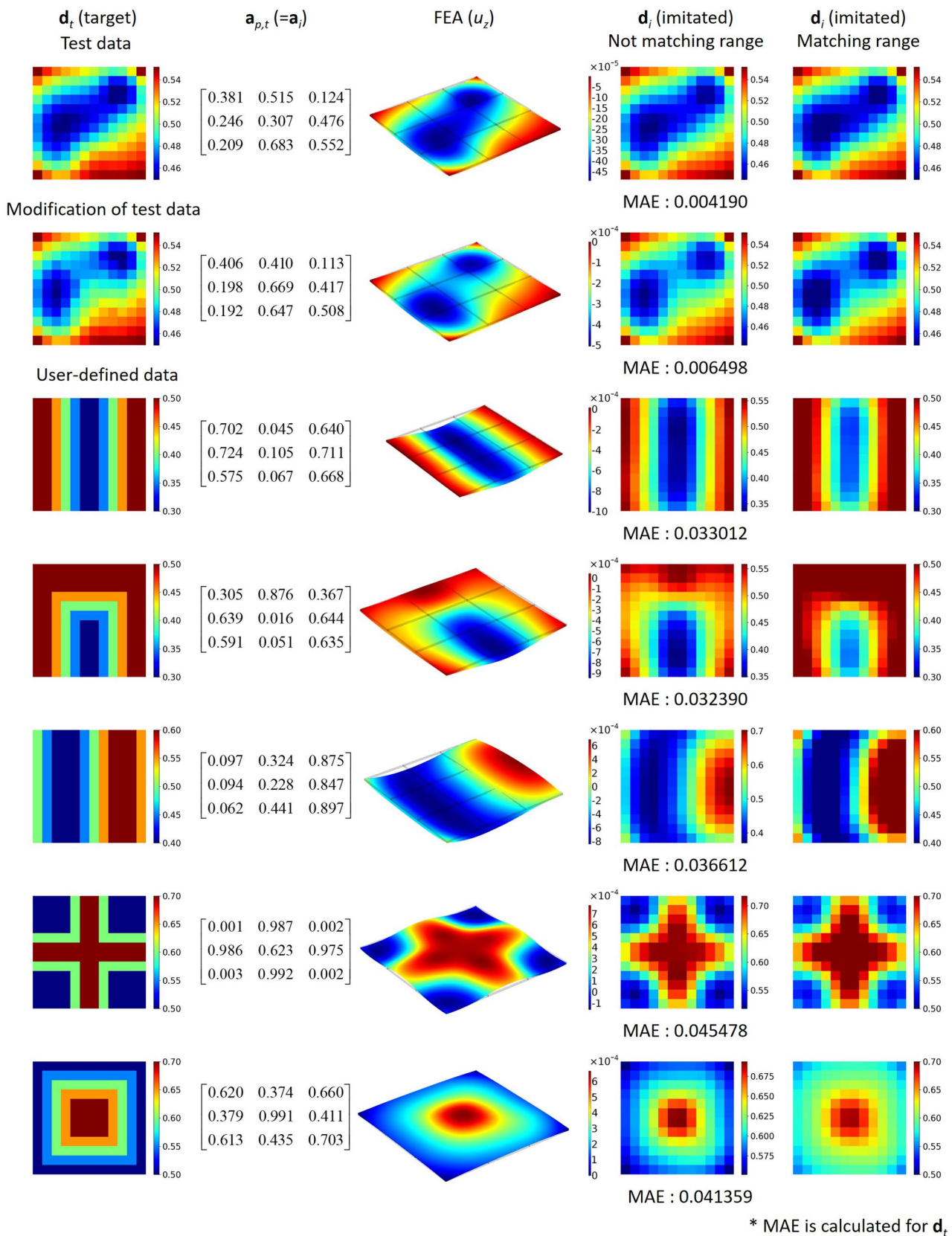


Fig. 31 Determination of voltage condition using the ANN for inverse mapping trained with noise for the target normalized displacement matrix d_t

the appropriate voltage condition for the target displacement field guaranteed as a result of FEA. However, when an arbitrary displacement field was given as the target, the first approach was more effective.

This study has some limitations in terms of generalization because it dealt with the FEA and ANN for the specific DEA configuration. Therefore, it is necessary to expand the present work and consider various DEA shapes, electrode arrangements, and voltage ranges in the future. For example, in the present study, the divided regions for voltage application were set to 3×3 , but increasing the number of divided regions can implement more complex deformed surfaces. Additionally, the number of image pixels for the displacement field can be further increased for the precise design of the DEA. The usability of the presented voltage condition determination method can be maximized when collaborating with experimental studies.

In some situations, it is possible for a designer to find an appropriate voltage condition of DEA through empirical knowledge and trial and error, rather than cumbersome ANN modeling. In addition, a fine-tuning process by a designer may be required to determine the voltages more accurately after obtaining an appropriate voltage condition through the ANN-based approaches. However, as the correlation between voltage conditions and deformation becomes more complicated, the need for the data-driven prediction model will increase. In this case, a larger ANN model and more data will be required. The authors anticipate that ANN-based learning techniques will be effectively applied to complex and diverse DEA designs in the future.

Acknowledgements This work was supported by the National Research Foundation of Korea (NRF) Grant funded by the Korea government (MSIT) (NRF-2019R1A2C2084974).

Author contributions Conceptualization and methodology: Ki Hyun Kim and Gil Ho Yoon; Investigation and writing: Ki Hyun Kim; Review: Gil Ho Yoon; Funding acquisition and supervision: Gil Ho Yoon. Corresponding author: Gil Ho Yoon (ghy@hanyang.ac.kr).

Funding Not applicable.

Data availability Not applicable.

Code availability Not applicable.

Declarations

Conflict of interest The authors declare that they have no conflict of interest.

Ethical approval Not applicable

Consent to participate Not applicable

Consent for publication Not applicable

Replication of results The presented results were mainly obtained using our Python codes and may be provided on reasonable request.

References

- Ashouri M, Khaleghian S, Emami A (2022) Reduced-order modeling of conductive polymer pressure sensors using finite element simulations and deep neural networks. *Struct Multidisc Optim*. <https://doi.org/10.1007/s00158-022-03237-6>
- Attard MM (2003) Finite strain—isotropic hyperelasticity. *Int J Solids Struct* 40(17):4353–4378. [https://doi.org/10.1016/S0020-7683\(03\)00217-8](https://doi.org/10.1016/S0020-7683(03)00217-8)
- Brown NK, Garland AP, Fadel GM et al (2022) Deep reinforcement learning for engineering design through topology optimization of elementally discretized design domains. *Mater Design*. <https://doi.org/10.1016/j.matdes.2022.110672>
- Carpi F, De Rossi D (2004) Dielectric elastomer cylindrical actuators: electromechanical modelling and experimental evaluation. *Mater Sci Eng C* 24(4):555–562. <https://doi.org/10.1016/j.msec.2004.02.005>
- Carpi F, Migliore A, Serra G et al (2005) Helical dielectric elastomer actuators. *Smart Mater Struct* 14(6):1210–1216. <https://doi.org/10.1088/0964-1726/14/6/014>
- Carpi F, Salaris C, De Rossi D (2007) Folded dielectric elastomer actuators. *Smart Mater Struct* 16(2):300–305. <https://doi.org/10.1088/0964-1726/16/2/S15>
- Carpi F, Frediani G, Nanni M et al (2011) Granularly coupled dielectric elastomer actuators. *Ieee-Asme Trans Mechatron* 16(1):16–23. <https://doi.org/10.1109/Tmech.2010.2073714>
- Deng CY, Wang YZ, Qin C, et al. (2022) Self-directed online machine learning for topology optimization. *Nat Commun*. ARTN 388 10.1038/s41467-021-27713-7, <Go to ISI>://WOS:000744588000009
- Duduta M, Wood RJ, Clarke DR (2016) Multilayer dielectric elastomers for fast, programmable actuation without prestretch. *Adv Mater* 28(36):8058–8063. <https://doi.org/10.1002/adma.201601842>
- Guo XX, Li W, Iorio F (2016) Convolutional neural networks for steady flow approximation. In: Kdd'16: Proceedings of the 22nd Acm Sigkdd International Conference on Knowledge Discovery and Data Mining pp 481–490. <https://doi.org/10.1145/2939672.2939738>
- Hajiesmaili E, Clarke DR (2019) Reconfigurable shape-morphing dielectric elastomers using spatially varying electric fields. *Nat Commun*. <https://doi.org/10.1038/s41467-018-08094-w>
- Henann DL, Chester SA, Bertoldi K (2013) Modeling of dielectric elastomers: design of actuators and energy harvesting devices. *J Mech Phys Solids* 61(10):2047–2066. <https://doi.org/10.1016/j.jmps.2013.05.003>
- Kingma DP, Ba JL (2014) Adam: A method for stochastic optimization. In: Proceedings of the 3rd International Conference for Learning Representations, San Diego, CA, May 7–9, 2015
- Kofod G, Pajanen M, Bauer S (2006) New design concept for dielectric elastomer actuators. *Smart Struct Mater* 10(1117/12):674557
- Krizhevsky A, Sutskever I, Hinton GE (2017) Imagenet classification with deep convolutional neural networks. *Commun Acm* 60(6):84–90. <https://doi.org/10.1145/3065386>
- Kumar A, Vadlamani NR (2021) Inverse design of airfoils using convolutional neural network and deep neural network. In: Proceedings of Asme 2021 Gas Turbine India Conference (Gtindia2021) <Go to ISI>://WOS:000883533100004
- Larson C, Spjut J, Knepper R et al (2019) A deformable interface for human touch recognition using stretchable carbon nanotube

- dielectric elastomer sensors and deep neural networks. *Soft Robot* 6(5):611–620. <https://doi.org/10.1089/soro.2018.0086>
- Lee XY, Balu A, Stoecklein D et al (2019) A case study of deep reinforcement learning for engineering design: Application to microfluidic devices for flow sculpting. *J Mech Design* 10(1115/1):4044397
- Lei X, Liu C, Du ZL et al (2019) Machine learning-driven real-time topology optimization under moving morphable component-based framework. *J Appl Mech Trans Asme* 10(1115/1):4041319
- Liang L, Liu ML, Martin C et al (2018) A deep learning approach to estimate stress distribution: a fast and accurate surrogate of finite-element analysis. *J R Soc Interface*. <https://doi.org/10.1098/rsif.2017.0844>
- Liu DJ, Tan YX, Khoram E et al (2018) Training deep neural networks for the inverse design of nanophotonic structures. *Acs Photon* 5(4):1365–1369. <https://doi.org/10.1021/acsp Photonics.7b01377>
- Messner MC (2020) Convolutional neural network surrogate models for the mechanical properties of periodic structures. *J Mech Design* 10(1115/1):4045040
- Nair V, Hinton GE (2010) Rectified linear units improve restricted boltzmann machines. In: *Proceedings of the 27th International Conference on Machine Learning*, Haifa, Israel, June 21–24, pp 807–814
- Nie ZG, Jiang HL, Kara LB (2020) Stress field prediction in cantilevered structures using convolutional neural networks. *J Comput Inf Sci Eng* 10(1115/1):4044097
- Pelrine R, Kornbluh R, Joseph J et al (2000) High-field deformation of elastomeric dielectrics for actuators. *Mater Sci Eng C* 11(2):89–100. [https://doi.org/10.1016/S0928-4931\(00\)00128-4](https://doi.org/10.1016/S0928-4931(00)00128-4)
- Pelrine RE, Kornbluh RD, Joseph JP (1998) Electrostriction of polymer dielectrics with compliant electrodes as a means of actuation. *Sens Actuators A* 64(1):77–85. [https://doi.org/10.1016/S0924-4247\(97\)01657-9](https://doi.org/10.1016/S0924-4247(97)01657-9)
- Shian S, Diebold RM, Clarke DR (2013) Tunable lenses using transparent dielectric elastomer actuators. *Opt Express* 21(7):8669–8676. <https://doi.org/10.1364/Oe.21.008669>
- Shian S, Bertoldi K, Clarke DR (2015) Dielectric elastomer based grippers for soft robotics. *Adv Mater* 27(43):6814–+. <https://doi.org/10.1002/adma.201503078>
- Shih B, Shah D, Li JX et al (2020) Electronic skins and machine learning for intelligent soft robots. *Sci Robot*. <https://doi.org/10.1126/scirobotics.aaz9239>
- Sui FP, Guo RQ, Zhang ZZ et al (2021) Deep reinforcement learning for digital materials design. *Acs Mater Lett* 3(10):1433–1439. <https://doi.org/10.1021/acsmaterialslett.1c00390>
- Sun ZY, Wang YG, Liu P et al (2022) Topological dimensionality reduction-based machine learning for efficient gradient-free 3d topology optimization. *Mater Design*. <https://doi.org/10.1016/j.matdes.2022.110885>
- Wang HM, Cai SQ, Carpi F et al (2012) Computational model of hydrostatically coupled dielectric elastomer actuators. *J Appl Mech Trans Asme* 10(1115/1):4005885
- Weeratunge H, Shireen Z, Iyer S et al (2022) A machine learning accelerated inverse design of underwater acoustic polyurethane coatings. *Struct Multidisc Optim*. <https://doi.org/10.1007/s00158-022-03322-w>
- Ye ZH, Chen Z (2017) Self-sensing of dielectric elastomer actuator enhanced by artificial neural network. *Smart Mater Struct* 26(9):ARTN 095056. [10.1088/1361-665X/aa7e66](https://doi.org/10.1088/1361-665X/aa7e66)
- Yu Y, Hur T, Jung J et al (2019) Deep learning for determining a near-optimal topological design without any iteration. *Struct Multidisc Optim* 59(3):787–799. <https://doi.org/10.1007/s00158-018-2101-5>
- Zhang T, Wang J, Liu Q et al (2019) Efficient spectrum prediction and inverse design for plasmonic waveguide systems based on artificial neural networks. *Photon Res* 7(3):368–380. <https://doi.org/10.1364/Prj.7.000368>
- Zheng S, Fan HJ, Zhang ZY et al (2021) Accurate and real-time structural topology prediction driven by deep learning under moving morphable component-based framework. *Appl Math Model* 97:522–535

Publisher's Note Springer Nature remains neutral with regard to jurisdictional claims in published maps and institutional affiliations.

Springer Nature or its licensor (e.g. a society or other partner) holds exclusive rights to this article under a publishing agreement with the author(s) or other rightsholder(s); author self-archiving of the accepted manuscript version of this article is solely governed by the terms of such publishing agreement and applicable law.